



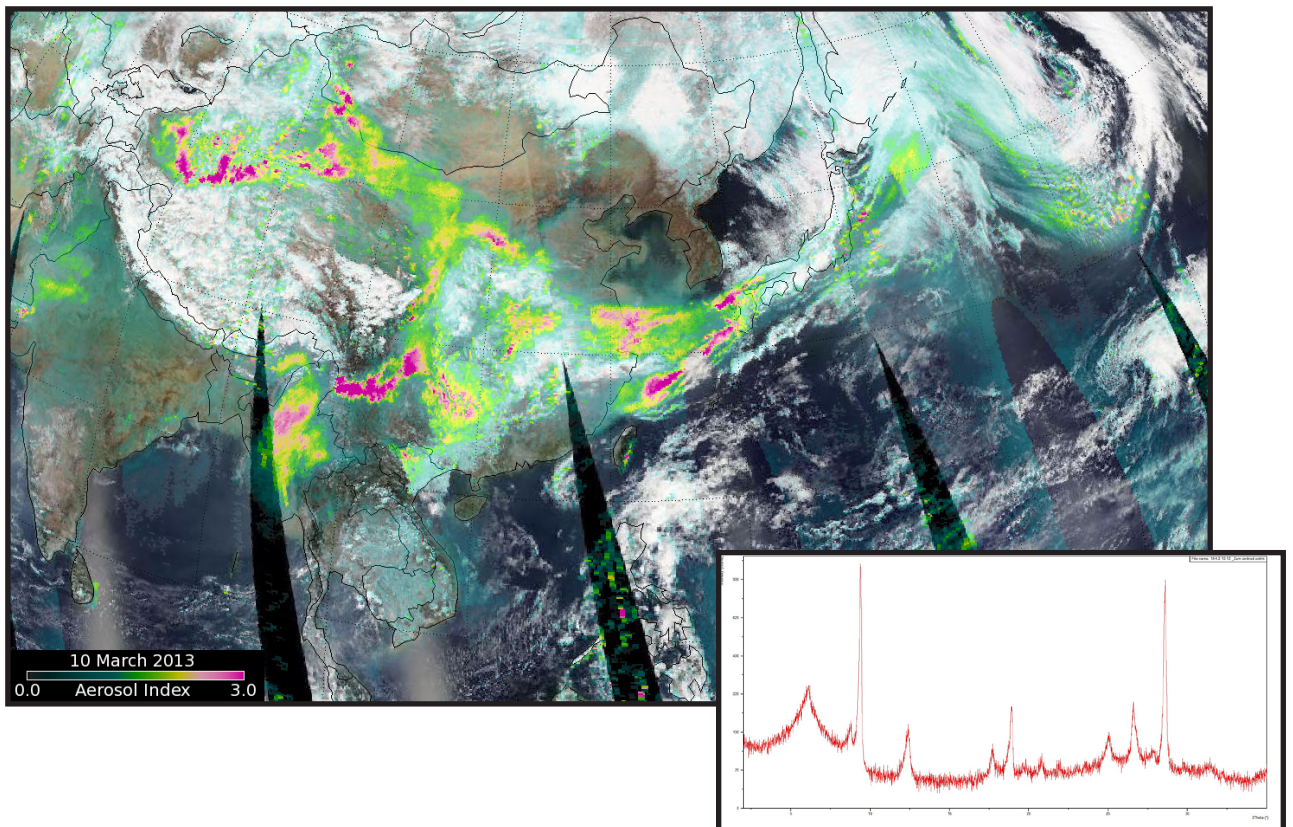
Stockholm
University

Master Thesis

Degree Project in
Marine Geology 60 hp

Mineralogy and grain size of eolian sediments from the Shatsky Rise, NW Pacific Ocean: mineralogy as proxy for eolian record comparisons

Therese Granberg



Stockholm 2015

Department of Geological Sciences
Stockholm University
SE-106 91 Stockholm
Sweden

Abstract

The East Asian monsoon system affects global climate since it is a main part of the atmospheric system. Loess-paleosoil sequences on the Chinese Loess Plateau (CLP) are valuable climatic archives formed through changed monsoonal settings creating alternating periods of wet and dry climate. During the winter monsoon season the westerlies transports mineral dust from the Asian deserts to the CLP and over the North Pacific Ocean. The eolian fraction of North Pacific sediments should therefore constitute the distal fraction of the loess sequence, which is currently not sufficiently dated for as high-resolution paleoclimatic studies as desired. Dating improvements of loess-paleosoil sequences through correlations with uniformly and reliably dated marine sediments have previously been successful, but not without complications that arise when different proxies are used for the correlation. The objectives of this study are to use mineralogy, obtained through XRD analyses, as a common proxy in order to investigate whether the eolian fraction of marine sediments from ODP Site 1208A on the central Shatsky Rise, NW Pacific Ocean, displays similar origin and mineralogical changes at ~ 2.6 Ma as a red clay-loess/paleosoil sequence from Lingtai, central CLP. The mineralogical record from Site 1208A will also be compared to those obtained from the North Pacific Moana Wave and ADIOS dust cruises and ODP Sites 885A/886B. A methodological objective is to evaluate whether using adjustable or fixed XRD divergence slit settings will affect the mineralogical interpretations.

This study presents mineralogical and grain size data obtained through XRD respectively laser diffraction analyses of the $<2\mu\text{m}$ and $2\text{-}20\mu\text{m}$ fraction of two eolian sediments sequences ($\sim 0\text{-}165.3$ k.y and $\sim 2.27\text{-}2.91$ m.y) from Site 1208A. No major mineralogical or grain size changes have been observed between the upper and lower section, or at ~ 2.6 Ma. This could be due to the relatively limited samples and obscuration of the purely terrigenous signal by ash contribution and alteration at Site 1208A. On the other hand, any prominent mineralogical changes at 1208A may have occurred prior to the investigated time period, as has been determined at the North Pacific ODP Sites 885A/886B at 3.8 Ma. Even though the eolian sources were developed prior to ~ 2.6 Ma, dust deposition on the CLP was reduced during the late Pliocene compared to the early Pleistocene due to different meteorological conditions. These conditions would not have precluded eolian deposition over the North Pacific Ocean.

Some less prominent differences could be observed between the upper and lower section at 1208A. The upper section shows higher concentrations of kaolinite, chlorite and quartz in the $<2\mu\text{m}$ fraction, and lower concentrations of illite, kaolinite and chlorite in the $2\text{-}20\mu\text{m}$ fraction than the lower section. The $<2\mu\text{m}$ and $2\text{-}20\mu\text{m}$ fraction generally display larger grain size, lower clay and higher sand concentrations, and lower skewness values in the lower than upper section, inferably due to more relatively coarse ash. Adjustable and fixed XRD slit settings resulted in similar interpretations of talc and quartz in monomineralic samples.

The compared sites show mineralogical similarities, and most of the differences could be explained by different transportation distances from the Asian sources and varying input of volcanic material, despite deviating age models, resolutions, laboratory and analytical techniques. Similar origin of the eolian sediments from Site 1208A and Lingtai could be inferred in this study. This indicates that using mineralogy as a common comparative proxy may facilitate correlations of the marine and terrestrial realms for further dating refinements of the CLP, and extend our paleoclimatic knowledge of Eastern Asia.

Table of Contents

Abstract	1
1. Introduction	4
1.1 The East Asian monsoon system	4
1.2 Mineral dust and surficial marine sediments.....	4
1.3 Size and compositional alteration of mineral dust.....	5
1.4 Objectives and hypotheses	5
2. Background	7
2.1 Site 1208A.....	7
2.1.1 Origin and oceanography.....	7
2.1.2 Lithology.....	7
2.1.3 Sediment and mass accumulation rates.....	8
2.1.4 Deposition and alteration.....	8
2.1.5 Ash layers.....	8
2.2. X-ray diffraction	9
2.2.1 X-ray diffraction theory	9
2.2.2 X-ray diffraction technique	10
3. Materials and methods	11
3.1 Sample selection.....	11
3.2 Pre-treatment procedures.....	11
3.2.1 Carbonate removal	11
3.2.2 Size fractionation and Mg saturation	12
3.2.3 Homogenization and talc spiking	12
3.2.4 Sample mounting.....	12
3.3 XRD analyses.....	13
3.3.1 XRD measurements.....	13
3.3.2 Mineral identification and peak area determination.....	13
3.4. Data treatments.....	14
3.4.1 Weight % conversion	14
3.4.2 Peak area ratios	14
3.4.3 Mass accumulation rates.....	15
3.4.4 Statistical analyses	15
3.5. Fixed and adjustable XRD divergence slit comparison	16
3.6 Grain size analyses	18
4. Results	19
4.1 1208A mineralogy and grain size.....	19
4.1.1 Mineralogy.....	20
4.1.2 Grain size	23
5. Discussion	27
5.1 Paleoclimatic and volcanogenic factors	27
5.1.1 Weathering conditions and mineralogy of the Asian source areas	27

5.1.2 Transportation pathways and wind strength.....	27
5.1.3 Contribution and alteration of volcanic material.....	28
5.1.4 Bioturbation.....	28
5.2 1208A mineralogical and grain size interpretations	29
5.2.1 Mineralogy.....	29
5.2.2 Grain size.....	30
5.3 Comparative settings.....	31
5.4 General influential factors for proxy record comparisons	37
5.4.1 Age models and resolutions	37
5.4.2 Laboratory techniques.....	39
5.4.3 Analytical techniques	39
5.5 Mineralogical comparison between 1208A and previous eolian studies	41
5.5.1 Transportation time and distance.....	43
5.5.2 Volcanic contribution.....	44
5.5.3 Mixing of dust from different source areas.....	44
6. Conclusions	45
7. Acknowledgments	46
8. References	47
9. Appendices.....	53

1. Introduction

1.1 The East Asian monsoon system

The East Asian monsoon is a main constituent of Earth's atmospheric circulation system capable of immense energy transfer, which strongly affects global climate. Variations in solar insolation, global ice volume and tectonic uplifting affect the East Asian monsoon, causing varying periods of comparatively wet and arid climatic conditions in eastern Asia. These changing monsoonal settings form loess-soil sequences on the Chinese Loess Plateau (CLP), which are continental windblown silt deposits interbedded with altered palaeosoils that serve as highly useful terrestrial climatic archives (Gylesjö and Arnold, 2006).

Seasonal intensity changes of the East Asian monsoon system lead to periodic exposure of these continental deposits to vigorous winds that entrain mineral dust. During summer, a high-pressure system develops over the western Pacific Ocean (Pacific High), and another over the southern Indian Ocean. Meanwhile, a low-pressure system forms over southern Asia, resulting in warm, moist winds traveling from the south-southeast over the continent. During winter, a high-pressure system develops over Siberia (Siberian High), and a low-pressure system forms over the northwest Pacific Ocean (Aleutian Low), resulting in cold, dry dust carrying winds traveling from the north-northwest over central China (Fig. 1). The East Asian summer and winter monsoon systems are responsible for some of the most dynamic interactions between the continental, oceanic and atmospheric systems on Earth (Liu and Ding, 1998).

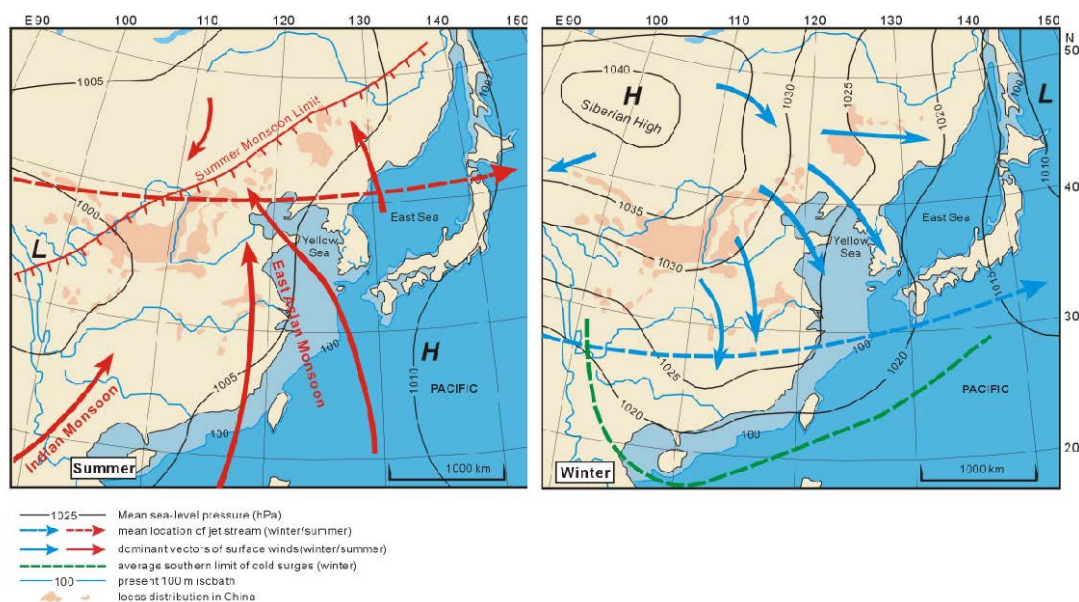


Figure 1. Seasonal changes in the wind system of the East Asian monsoon area (Yancheva *et al.*, 2007. Accessed 27 January, 2015, modified in PowerPoint)

1.2 Mineral dust and surficial marine sediments

Asia is the main source of mineral dust reaching the North Pacific Ocean, from the tropics to the mid-latitudes. The monsoonal intensity fluctuations trigger the highest seasonal activity of dust storms and the prevailing westerlies during springtime, resulting in maximum dust fluxes to the northern Pacific from February to June (Muhs, 2013; Uematsu *et al.*, 1983). Central Pacific equatorial regions receive $\sim 10 \text{ mg/cm}^2/\text{k.y.}$,

central North Pacific ~ 100 mg/cm²/k.y., and northwest Pacific off the coast of Japan ~ 1000 mg/cm²/k.y. These fluxes are highly similar to contemporaneous eolian sedimentation rates, specifically central Pacific equatorial regions accumulate ~ 25 mg/cm²/k.y., central North Pacific ~ 100 mg/cm²/k.y., and northwest Pacific off the coast of Japan ~ 1000 mg/cm²/k.y. (Rea, 1994). Several studies have also shown statistical similarity between the average mineralogy of North Pacific mineral dust and underlying surficial sediments (Prospero, 1981; Ferguson *et al.*, 1970; Blank *et al.*, 1985). Blank *et al.*, 1985, found the smectite group to be an exception, but concluded low abundance, under-sampling of atmospheric dust collector and low analytical precision of smectite as probable causes of the reported dissimilarity.

Analyses of the mineralogical composition of dust and marine surface sediments provide indications of potential source areas and their weathering regimes, because the mineralogy of continental surface deposits displays regional variations caused by compositional differences in the underlying geology and weathering conditions. Clay minerals are mainly formed by chemical weathering processes and primary minerals, such as quartz and plagioclase, are dominantly formed by physical weathering processes (Chamley, 1989).

1.3 Size and compositional alteration of mineral dust

Climate and geology control the basic zonal distribution of eolian mineral assemblages in oceanic basins, but other influential factors such as long distance transport by wind and ocean currents can significantly alter the mineralogical composition in relation to the continental source area (Chamley, 1989). These transportation processes cause size fractionation of the mineral assemblage due to gravity settling of coarse grains. Moreover, size fractionation causes contemporary compositional fractionation, leading to successively larger relative proportions of clay minerals as opposed to primary minerals such as quartz and plagioclase (Arnold *et al.*, 1998). It is therefore necessary to analyze identical size fractions when performing comparative mineralogical studies of dust and marine sediments. For example, Leinen *et al.*, 1994, have reported the same main mineral phases to be present in the <2µm and 2-20µm fractions of mineral dust collected over the North Pacific Ocean, specifically illite, smectite, kaolinite, chlorite, quartz and plagioclase. However, the differences in mineral phase proportions turned out to be greater between the size fractions than between the northwest and northeast regions of the Pacific Ocean. Illite is predominant in both size classes. The most evident differences are that the 2-20µm fraction is relatively enriched in quartz and plagioclase, whereas the <2µm fraction is relatively enriched in kaolinite.

1.4 Objectives and hypotheses

The CLP provides an excellent opportunity to study how the East Asian monsoon system has changed throughout Earth's history, but high-resolution age models have proven difficult to establish. This has limited most chronologies to rely on paleomagnetic reversal stratigraphies, which occasionally have been tuned to astronomical parameters (Ding *et al.*, 1999). Due to its downwind location from the CLP Shatsky Rise should receive the distal fraction of the loess sequence (Hovan *et al.*, 1991). Dating techniques for marine sediments are relatively uniform and reliable, which makes them advantageous for palaeoclimatic studies. Dating refinements of sediment sequences from the CLP have previously been accomplished through correlations with the marine sediments from the Shatsky Rise. Hovan *et al.*, 1989, enabled direct linkage of the Xifeng loess-soil sequence to the well-established marine δ¹⁸O timescale through correlation

with an eolian flux record obtained from core V21-146 from the Shatsky Rise in the northwestern Pacific Ocean. This resulted in age refinement of the last 500 k.y. of the Xifeng loess-soil sequence. Further successful dating improvements of loess-soil sequences from the CLP are desirable in order to deepen our paleoclimatic knowledge of eastern Asia.

Gylesjö and Arnold, 2006, conducted a mineralogical study of the $<2\mu\text{m}$ and $2-20\mu\text{m}$ fraction of a red clay-loess/paleosoil sequence at Lingtai, central CLP. Both the red clay and the loess/paleosoil are eolian sediments. At the transition between the underlying red clay and overlying loess, at 2.6 Ma, they determined higher average concentrations of quartz, kaolinite and chlorite in the red clay, and abrupt changes in the smectite and kaolinite concentrations in the $<2\mu\text{m}$ fraction.

I have conducted a mineralogical and grain size study through X-ray diffraction respectively laser diffraction analyses of the $<2\mu\text{m}$ and $2-20\mu\text{m}$ eolian fraction of marine sediments from ODP Site 1208A located on the central Shatsky Rise in the northwestern Pacific Ocean. The objectives are to; (i) interpret the mineralogy and grain size of sediment sequences from Site 1208A; (ii) compare the mineralogy of Site 1208A with the mineralogy of the red clay-loess/paleosoil sequence at Lingtai, mineral dust collected over the northern Pacific Ocean and sediment sequences from ODP Sites 885A and 886B located in the northern Pacific Ocean; (iii) evaluate whether mineralogy can serve as a useful proxy for determining if the mineralogy of both Site 1208A and Lingtai has similar origin; (iv) finally, evaluate whether using fixed or adjustable XRD divergence slits will affect the mineralogical interpretations. This last methodological objective was chosen since the latest technique with adjustable slit settings has been used in this study whereas fixed slit settings have been used in the comparing eolian studies. I have tested the following hypotheses:

1. The eolian sediment sequence from Site 1208A has similar mineralogical composition as the Lingtai sequence, eolian sediments from Sites 885A and 886B in the northern Pacific Ocean, and mineral dust collected over the northern Pacific Ocean.
2. There is a mineralogical change in the $<2\mu\text{m}$ fraction at ~ 2.6 Ma at Site 1208A.
3. Similar origin of the sediments from Site 1208A and Lingtai can be determined through X-ray diffraction analyses of their mineralogical compositions.
4. Interpretations of relative mineral abundances are the same whether adjustable or fixed X-ray diffraction slit widths are used.

2. Background

2.1 Site 1208A

2.1.1 Origin and oceanography

Shatsky Rise is a large igneous province in the northwestern Pacific Ocean, approximately 1000 miles off the east coast of Japan (Evans *et al.*, 2005). It was formed by several volcanic eruptions at a hotspot triple junction, between 146 and 133 Ma in the early Cretaceous. This early formation conceivably makes Shatsky Rise the oldest oceanic plateau on Earth today (Bown, 2006). Tamu Massif, the largest feature of Shatsky Rise, has recently been confirmed as the biggest single shield volcano discovered on Earth so far (Sager *et al.*, 2013). Shatsky Rise comprises three main topographic highs: the northern, central and southern highs, providing a sedimentary record spanning from the Cretaceous through the Cenozoic (Evans *et al.*, 2005). Site 1208A is located close to the center of the central high, $36^{\circ}7.6301' \text{ N}$, $158^{\circ}12.0952' \text{ E}$, (Fig. 2) above the nepheloid layer at a water depth of 3346 m (Bralower *et al.*, 2002). This location has not received ice-rafted debris during glacial or interglacial periods, and lies far from the continental sources of hemipelagic sedimentation (Rack *et al.*, 1995).

The Kuroshio Current System is the western boundary current of the North Pacific anticyclonic subtropical gyre. In the offshore region east of Japan, this current flowing to the northeast merges with the subarctic Ovasio Current traveling to the southwest. This convergence generates meanders into the Kuroshio Current as it progresses eastward into the northwestern Pacific Ocean as the Kuroshio Current Extension. Site 1208A is situated underneath this extending current. Three quarters of its volume flows northeasterly around the northern and central highs, whereas the remainder flows easterly between the southern and central highs (Venti, 2011).

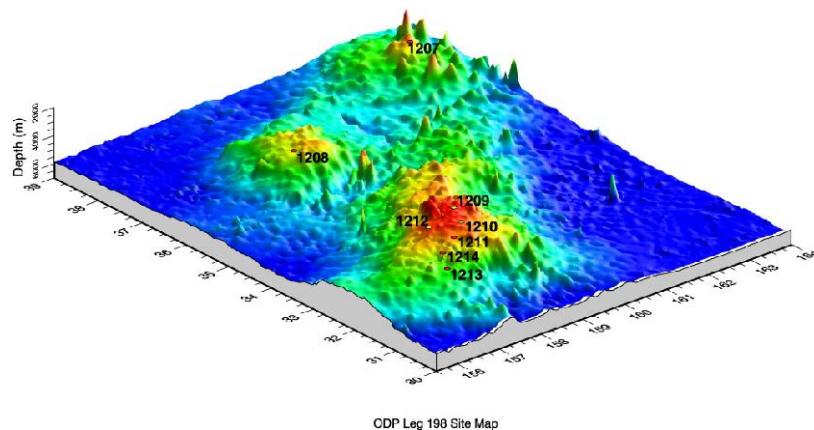


Figure 2. Bathymetric map of Shatsky Rise displaying the sites drilled during ODP Leg 198 (ODP Volume 198 Initial Reports, 2002, http://www-odp.tamu.edu/publications/198_IR/198TOC.HTM. Accessed 20 January 2015).

2.1.2 Lithology

Two major lithostratigraphic units have been recovered from 1208A, reaching a total sediment thickness of 345.9 m. Unit I constitutes a Holocene-Paleocene sequence composed of lighter and darker interchanging nannofossil ooze and nannofossil clay, with the additional presence of radiolarians and diatoms. Further division of Unit I into

subunits IA, IB and IC is based on slightly gradational downcore changes in nature and composition of these interchanging intervals. Unit II is a Campanian-Albian sequence comprised of nannofossil ooze with small amounts of chert.

The samples analyzed in this study are exclusively from Subunit IA, which extends from 0 to 251.6 mbsf without unconformities. This subunit has an average recovery rate of 100.1%, caused by minor core expansion. No signs of drilling deformation are displayed by the interval extending from 0 to 185.2 mbsf, incorporating the samples in this study. Characteristic features of Subunit IA include: moderate amounts siliceous microfossils, ash layers and various forms of pyrite. These sediments are predominantly greenish gray in color, and display subhorizontal color banding in both the lighter and darker lithologies (Bralower *et al.*, 2002). Appendix A provides core photos and visual descriptions of the relevant core sections of Subunit IA.

2.1.3 Sediment and mass accumulation rates

The linear sedimentation rate at 1208A was 22.3 m/m.y. prior to ~ 3.0 Ma, whereupon it increased to 42.4 m/m.y. late in the early Pliocene. The carbonate fraction did not increase significantly at the time, which implies the increased noncarbonate fractions responsible for these enhanced sedimentation rates (Bralower *et al.*, 2002).

In order to avoid obscuration of the paleoclimatic signal by biogenic sedimentary components, eolian fluxes can be stated as mass accumulation rates (MARs) (Hovan *et al.*, 1989). The MAR of the bulk sediment was ~ 3.2 g/cm²/k.y. in the lower Pliocene, whereupon it decreased to ~ 2.4 g/cm²/k.y. in the Pleistocene. Carbonate and noncarbonate fractions contribute variably, but similarly, to the bulk mass by average MARs of 1.5 and 1.4 g/cm²/k.y., respectively throughout the late early Pliocene-Pleistocene time period (Bralower *et al.*, 2002).

2.1.4 Deposition and alteration processes

Subunit IC has been seismically interpreted as a drift deposit created by current redistribution, which is supported by the exceptionally high Neogene-Quaternary sedimentation rates. Subunits IA and IB, on the other hand, do not display evident sedimentological features of drift deposition, for instance contourites or winnowed lags (Bralower *et al.*, 2002).

Bioturbation may alternatively have destroyed subtle foraminiferal lags indicative of winnowing, suggested by the homogenous to moderately bioturbated appearance of Subunit IA. Bioalteration was however not intense enough to fully diffuse the present ash layers, and signs of winnowing seem therefore unlikely to have been destroyed in this manner. This assumes that organisms did not avoid the ash. More distinctive alteration features include high-angle contacts in the uppermost unit section, inferably created by erosion. Pyrite is present in various forms, mostly as pods and bands within burrow fills, but also as hard concretions (Bralower *et al.*, 2002).

2.1.5 Ash layers

The onset of widespread Northern Hemisphere glaciation ~ 2.6 Ma coincides with a global increase in volcanism, which is presented in Subunit IA as the highest abundance of vitric ash layers within the whole sediment sequence. Colorless glass constitutes the main ash component, and crystalline phases contribute in low amounts. Among these, plagioclase predominates through a maximum of 12% of the total composition, yet averages <3%. Additional mineral phases occurring as trace amounts include pyrite,

amphibole, biotite, k-feldspar, pyroxene and quartz. Ash textures range from blocky to bubble-wall and pumice (Gadley and Marsaglia, 2005).

Multiple volcanic sources are suggested by the heterogeneous ash texture and composition. The Japan and Kurile arcs are potential sources of airborne ash, and the Izu-Bonin arc system is the most likely source of abraded ash and pumice, carried northward by the Kuroshio Current. This pumice origin is supported by high vesicularity of samples from both the Izu-Bonin arc and Site 1208A (Gadley and Marsaglia, 2005).

2.2 X-ray diffraction

2.2.1 X-ray diffraction theory

In July 1919, Albert W. Hull wrote: "All that one needs to use in a chemical analysis is the fact that every crystalline substance gives a pattern; that the same substance always gives the same pattern; that no two different substances give the same pattern; and that in a mixture of substances each produces its pattern independently of the others" (Hull, 1919). What Hull referred to here is a mineral's characteristic diffraction pattern, generated through X-ray irradiation. These are characteristic because interplanar spacings of crystal lattices are specific to each mineral. Diffraction patterns are therefore used as fingerprints for identifying unknown mineral phases. This is the fundamental concept behind X-ray diffraction (XRD) analysis.

X-rays used in XRD measurements have an approximate wavelength of 1 or 2 Å (1 Å = 10^{-8} cm), comparable to the interplanar spacings of atoms within most mineral structures. This dimensional similarity causes diffraction of X-rays by the crystal lattice. Diffracted X-rays will only be efficiently reflected if they experience constructive interference. For this condition to be met, the incident angle must be such that the extra distances covered by diffracted rays from successively deeper atomic planes within the crystal are equal to an integer number of wavelengths. The relationship between wavelength (λ), incident angle (θ) and interplanar spacing (d) is illustrated in Figure 3 and described by Bragg's equation:

$$n\lambda = 2d\sin\theta \quad (1)$$

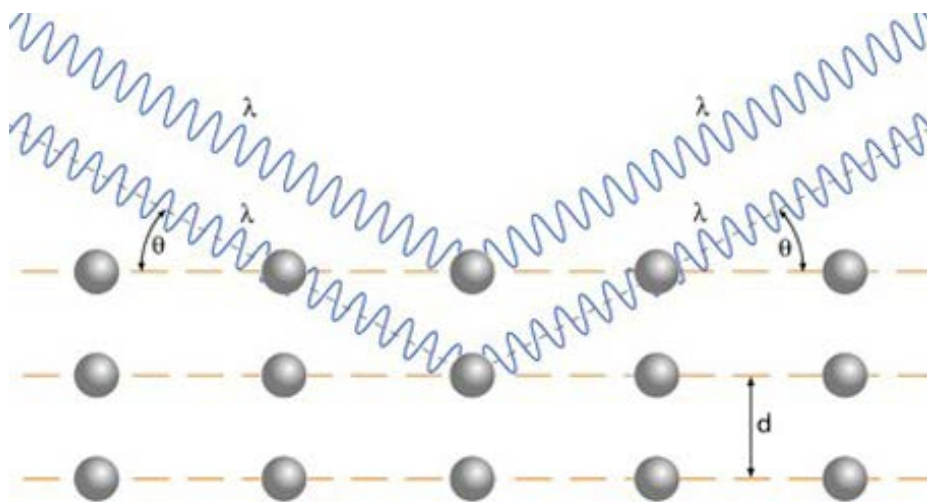


Figure 3. Schematic of diffraction of X-rays by a crystal lattice (PANalytical, 2015, <http://www.panalytical.com/Technology-background/Braggs-law.htm>, Accessed 20 January 2015).

X-rays not meeting these criteria experience destructive interference, and are therefore not observed. Hence, if an intensity peak is detected during measurements, the mineral structure has suitable d-spacings for reflecting X-rays at that particular angle of incidence. Each mineral contains several atomic planes at specific d-spacings potentially capable of diffraction. Among clay minerals, the largest structural variations occur along the Z-axis, therefore the most diagnostic d-spacings occur between the basal {001} planes. Characteristic clay mineral diffraction patterns display rational series of peaks generated from these basal planes, meaning they are evenly spaced at approximately 2θ-values of 40° or less. A pre-requisite for diagnostic diffraction patterns are preferred orientation of the clay minerals to enhance these basal peaks (Moore and Reynolds, 1997).

2.2.2 X-ray diffraction technique

A diffractometer is the instrument used for XRD measurements. Figure 4 is a schematic of the X-ray passage from the X-ray tube to the detector, however all diffractometers are not equipped with all displayed slits, filters and masks. The basics are that the X-ray beam is generated within a Cu-tube, after which it leaves through a beryllium window before passing the shutter opening. The beam then enters a divergence slit with fixed or adjustable widths, and a Soller slit, serving to constrain, focus and parallel the beam before reaching the sample surface. The divergence slit width regulates the irradiated sample surface area.

After diffracting, the beam passes a receiving slit regulating the resolution and sharpness of detected intensity peaks. The diffracted beam intensity is proportional to receiving slit width. Unfortunately, increased intensity is gained at the expense of resolution, but clay mineral reflections are weak and intrinsically broad, making these analyses require maximum intensity. Next, the beam passes a monochromator equipped with a curved graphite crystal with specific spacings arranged to diffract single wavelength radiation into the detector. The registered data are intensity (cps) and position (2θ angle) of each detected mineral peak, enabling mineral identification through comparisons with a reference mineral database. The graph of intensity versus 2θ angle is the diffraction pattern (diffractogram). Semi-quantitative estimates of mineral proportions are obtainable by peak area analysis. Ratios of different mineral peak areas are used in comparisons between samples (Moore and Reynolds, 1997).

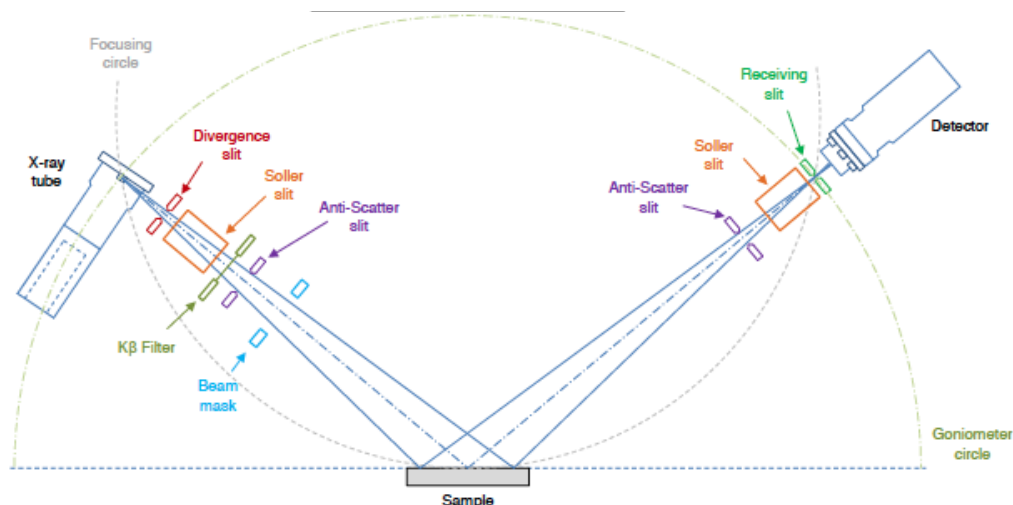


Figure 4. Schematic of the X-ray passage from the X-ray tube to the detector (RMS Foundation, 2013, <http://profex.doebelin.org/wp-content/uploads/2014/02/Lesson-2-Diffractometers-and-Phase-Identification.pdf>. Accessed 27 January 2015).

3. Materials and methods

3.1 Sample selection

The uppermost 24 m of Subunit 1A was previously size fractionated and processed for removal of iron oxides, carbonates and biogenic silica by S. Gylesjö in order to determine the eolian bulk MARs at Site 1208A during the last ~ 560 k.y. (Gylesjö, 2005). The amount of eolian material ranges between 22.7-73.3 wt.%, and averages 44.1 wt.%. The grain size and mineralogy of the <2 μ m and 2-20 μ m fraction of these samples corresponding to the last 165.3 k.y. (0.2-7.0 mbsf), have been analyzed in this study and will be referred to as the upper section. The age model is derived from shipboard magnetic reversal stratigraphy, foraminiferal and calcareous nannofossil biostratigraphies (Bralower *et al.*, 2002), and the age resolution is ~ 4 cm/k.y.

Another core section with an age interval of ~2.72-2.91 m.y. (107.3-132.8 mbsf) has been selected in order to primarily facilitate the comparison to the Lingtai sequence, and will be referred to as the lower section. The age model is derived from the Pliocene-Pleistocene benthic foraminiferal $\delta^{18}\text{O}$ stratigraphy by Venti and Billups, 2012, and the age resolution is ~ 5 cm/k.y. Venti and Billups, 2012, concluded that this $\delta^{18}\text{O}$ stratigraphy shows excellent agreement with the global $\delta^{18}\text{O}$ stack of Lisiecki and Raymo from 2005, which enables straightforward comparisons with other marine sites.

No mineral analysis has previously been conducted on the deeper samples. The total organic carbon ranges between 1.6-8.7 weight % and averages 6.0 weight % between 106.79-137.33 mbsf (Bralower *et al.*, 2002). No data of biogenic silica have been found for the deeper interval, but Robinson and Jenkyns, 2005, reported that the biogenic silica amount ranges between 1.8-16.4 weight % and averages 6.5 weight % between 190.53-318.77 mbsf. All biogenic silica is composed of opal-A, which has a very disordered crystal structure and is therefore nearly amorphous to X-rays. If it has not been removed it can generate a single diffuse broad hump centered around 4.1 Å (Elzea *et al.*, 1994; Jones and Segnit, 1971). I decided that organic matter and biogenic silica removal procedures involving relatively strong chemicals that could degrade fine clay particles with large reactive surfaces were not justified, but their potential presence was considered during the interpretations of the diffractograms.

3.2 Pre-treatment procedures

3.2.1 Carbonate removal

Initially, mortar and pestle were used to disaggregate and homogenize the deeper samples. The reported carbonate contents range between ~13-73 weight % (Bralower *et al.*, 2002). With the intention of ending up with ~1g eolian material after carbonate removal, the required sample mass were calculated and weighed on a four-digit scale before transfer into 250 ml Erlenmeyer flasks. Next, successive series of adding 150 ml of buffered acetic acid solution and placing the flasks on a shaker table for 2 h were conducted until no further reactions occurred. Centrifugation was thereafter implemented before the samples were oven dried at 30°C and finally weight registered.

3.2.2 Size fractionation and Mg saturation

Wet sieving through 63 μm sieves was conducted to separate the >63 μm and <63 μm fractions, and wet sieving through 20 μm sieves accompanied by insonication was subsequently conducted to separate the 2-20 μm and 20-63 μm fractions. Finally centrifugation was implemented in order to separate the <2 μm and 2-20 μm fractions. All size fractions were oven dried at 30°C and weight registered in order to determine their MARs. All of the following pre-treatments were conducted on both the shallow and deep samples. Mg saturation was achieved through three rounds of adding 1 N MgCl_2 saturated solution and centrifuging. This was done in order to reduce d-spacing variability in clay mineral crystal structures by substitution of exchangeable interstitial cations for Mg^{2+} . The samples were subsequently rinsed three times with deionized water, oven dried at 30°C and lastly weight registered.

3.2.3 Homogenization and talc spiking

The next pre-treatment steps included homogenizing and talc spiking the samples. The intensities of the minerals characteristic diffraction peaks can vary between samples due to differences in the total sample absorption coefficients. Adding a known mineral phase in unvarying amounts allows corrections for these intensity variations, which affects the variance between samples, but does not change the relative proportion of minerals within a sample (Chipera and Bish, 2013). Talc is suitable as an internal standard for clay mineralogy of marine sediments since its diagnostic peak is found within the same 2θ -range as those of the most common mineral components without causing peak interference.

The talc batch had previously been size fractionated into <2 μm and 2-20 μm . The samples were first completely wetted with acetone and homogenized with mortar and pestle. Subsequently, ~ 0.1 g sample and ~ 10 weight % talc were transferred to the mortar for further homogenization. Five sample replicates for the <2 μm and 2-20 μm fraction were made in order to determine the analytical precision of the major mineral constituents.

3.2.4 Sample mounting

A Millipore filtration system was used for sample mounting onto 0.45 μm Osmonics silver filters. Silver filters are commonly used for preparation of oriented clay mineral samples for XRD analyses because of their reusability, and the high atomic number of Ag creating comparably low background values (Poppe *et al.*, 1989). Initially, mounting was unsuccessful, probably due to oxidation of the filters caused by long-term storage. Different filter treatments were implemented, including insonication and overnight soaking in acetone, ammonium hydroxide and ethanol (Sterlitech Corporation, 2013). Overnight soaking in ethanol was successful when the filters were placed upright in 1 cm wide plastic core samplers for simultaneous soaking from both sides.

After the filter pre-treatment, sample mounting was initiated by flushing with deionized water to rinse the filters from possible ethanol remains, and to ensure efficient flow rates. The spiked samples were transferred into centrifuge tubes quarterly filled with deionized water, followed by 15-30 s each of vortexing, insonication and further vortexing. Thereafter, 1 ml of sample slurry was successively pipetted in a circular motion onto the funnel walls to distribute the sample evenly on the filter until an even sample cake was created. The mounted samples were then air dried before the analyses, except for the samples that cracked upon drying, which instead were analyzed wet immediately after remounting.

3.3 XRD analyses

3.3.1 XRD measurements

The filter-mounted samples were attached with double-sided adhesive tape onto sample holders in order to avoid movement during the analyses. In case of excessive sample thickness, adhesive paste was used to lower the sample surface in level with the holder edge. The analyses were conducted with PANalytical's X-ray diffraction system X'Pert³ Powder at the Department of Geological Sciences at Stockholm University. The samples were X-rayed from 2° to 35° 2θ, using CuKα radiation at 45 kV and 40 mA, at a rate of 0.02° 2θ/s, and with a spinning revolution of 1 s. Adjustable slit widths were used during measurements, but no anti-scatter slits or filters since these are no longer needed when a monochromator is used. After measuring air dried, the samples were placed in an ethylene glycol atmosphere for two nights to expand the swelling clays, and then re-measured at the same instrumental settings. The replicate measurements were run on the same day in order to avoid the effects of possible day-to-day instrumental deviations.

3.3.2 Mineral identification and peak area determination

Identification and peak area analyses of smectite, illite, kaolinite, chlorite, quartz, plagioclase and talc were made by using MacDiff 4.2.6 software, operating the single peak fitting technique applied with Split Pearson VII profile function (Petschick, 2010). The data were smoothed by three term simple moving average, and the background was found by calculation of every 70th point with 100 iterations for all 2θ values, and modified manually where needed.

Identification of smectite was made by removing the 14 Å chlorite peak in the glycolated sample from the 14 Å peak shared by chlorite and smectite in the air dried sample. Illite and quartz were identified by the 9.9 Å and 3.34 Å peaks respectively. Quartz was area corrected by subtracting 12 % of the 9.9 Å illite peak, due to the interfering 3.33 Å illite peak. The 3.58 Å kaolinite peak and the 3.54 Å chlorite peak form a complex at 24°-26° 2θ. The relative proportions of these diagnostic peaks were used for determining their relative contributions to the combined 7 Å peak area. Plagioclase and talc were identified by the ~ 3.2 Å and 9.33 Å peaks, respectively. The peak areas were then normalized to the diagnostic 9.33 Å talc peak area. An example of a diffraction pattern from the <2μm fraction is presented in Figure 5.

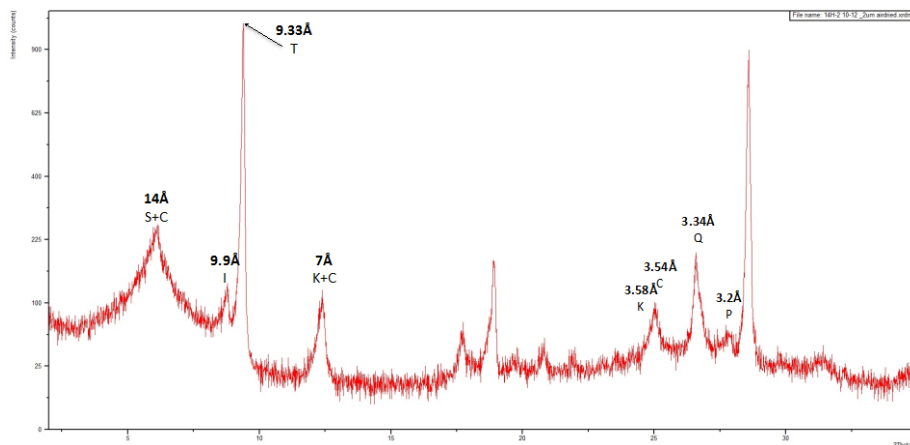


Figure 5. Diffraction pattern from sample 14H-2 10-12 (~ 2.6 Ma) of the <2μm displaying the diagnostic mineral peaks (Generated in PANalytical's software Data Viewer, modified in PowerPoint).

3.4 Data treatments

3.4.1 Weight % conversion

The main reason for converting peak areas into weight % is that the measured intensities are different for different minerals and not proportional to the mineral amounts. Peak area conversion thereby enables abundance estimations and mineralogical comparisons. This approach has been used to construct convenient distribution charts over the main minerals in oceanic basins (Heath and Pisias, 1979). Several methods have been developed that apply different weighting factors. The method by Biscaye, 1965, assumes that the sum of smectite, illite, kaolinite and chlorite is 100 % in each sample, which might be considered relatively applicable for the <2 μ m but not for the 2-20 μ m fraction. The weighting factors for converting the peak areas of illite (I), kaolinite (K), chlorite (C) and smectite (S) into relative weight percentages are 4, 2, 2 and 1, respectively (Biscaye, 1965). The weight percentages of kaolinite for instance in every sample are given by the equation:

$$kaolinite\ wt.\ \% = \frac{2K * 100}{2K + 2C + 4I + S} \quad (2)$$

With the use of 10 weight % talc internal standard, the Biscaye method from 1965 can be modified into the Corrected Biscaye method, which lets the sum of the clay minerals be 100 % solely for the sample with the highest value of 2K+2C+4I+S in the sample set (Heath and Pisias, 1979). This method allows for unidentified phases to be estimated. The weight percentages of kaolinite in every sample are then given by the equation:

$$kaolinite\ wt.\ \% = \frac{2K * 100}{(2K + 2C + 4I + S)_{max}} \quad (3)$$

The method by Heath and Pisias, 1979, uses a minimization technique for linear programming to convert normalized peak areas to weight %, which reduces the residual amorphous components. Their method is based specifically on North Pacific sediments and additionally enables estimates of quartz and plagioclase. The weighting factors for illite, kaolinite, chlorite and smectite are 75.2, 57.1, 8.5 and 8, respectively. The weighting factors for quartz and plagioclase are 9.2 and 49, respectively.

3.4.2 Peak area ratios

Mineralogical data can also be interpreted by evaluating the relative changes between the different minerals. The peak area ratios of kaolinite to illite (K/I) and kaolinite to chlorite (K/C) can be used as humidity indices, since kaolinite is commonly associated with strong hydrolysis during temperate/warm climatic conditions, whereas illite and chlorite formation are mainly favored during cold and dry climatic regimes. However, secondary formation of illite from micas may occur during humid and warm climatic conditions. The peak area ratio of smectite to illite (S/I) can similarly serve as a humidity index, although it may also reflect varying volcanic dust fluxes (Das *et al.*, 2013). Quartz to illite (Q/I) and plagioclase to illite (P/I) are peak area ratios of a primary mineral to a clay mineral. Since plagioclase is the main crystalline component of the ash at 1208A deviations between these ratios may indicate that plagioclase additionally has a volcanic origin.

3.4.3 Mass accumulation rates

Eolian MAR is a true measurement of mineral dust flux, and reflects the aridity fluctuations of the source areas (Xiao *et al.*, 2012). MARs of the bulk sediment were calculated by multiplying the linear sedimentation rate (LSR) with the dry bulk density (DBD) (equation 4). MARs of the eolian bulk material, 20-63 μm , 2-20 μm and <2 μm components were calculated by multiplying the MARs of the bulk sediment with the fraction of the separated size components after carbonate removal (equation 5). MARs of the major mineral components were subsequently calculated by multiplying the MARs of the <2 μm and 2-20 μm fraction with the estimated mineral abundances (equation 6). The fractions were attained by dividing the weight of the size component by the weight of the bulk sediment after carbonate removal. This procedure had not previously been conducted on the samples from the upper section, and MARs could therefore only be calculated for the samples from lower section. DBD values were determined using interpolation between laboratory measurements from Bralower *et al.*, 2002. LSRs for the lower section were calculated by interpolation between datums in the isotopic age model from Venti and Billups, 2012. The weight % of the unidentified material have been estimated by assuming that the whole sample equals 100 weight % and then subtracting the sum of the determined weight % of the major mineral components. These data are presented to highlight the potential significance of various components of the total sedimentary flux.

$$\text{MAR (g/cm}^2\text{/k.y.)} = \text{LSR (cm/k.y.)} \times \text{DBD (g/cm}^3\text{)} \quad (4)$$

$$\text{Size fractional MAR (g/cm}^2\text{/k.y.)} = \text{MAR (g/cm}^2\text{/k.y.)} \times \text{separated size component} \quad (5)$$

$$\text{Mineral MAR (g/cm}^2\text{/k.y.)} = <2\mu\text{m}/2\text{-}20\mu\text{m MAR (g/cm}^2\text{/k.y.)} \times \text{mineral wt.\%} \quad (6)$$

3.4.4 Statistical analyses

The software used for all statistical analyses were Microsoft Excel for Mac 2011, version 14.3.7. Significant differences between the <2 μm and 2-20 μm were determined by paired t-tests with a 95 % confidence interval. Significant differences between the sections and subsections within each size fraction, and between 1208A and the previous studies were determined by unpaired t-tests allowing unequal variances with a 95 % confidence interval.

3.5 Fixed and adjustable XRD divergence slit width comparison

Comparisons between XRD data obtained at fixed and adjustable slit settings cannot be made under the same conditions since the irradiated sample areas and volumes are not the same. Fixed slits generate measurements of a constant sample volume, whereas adjustable slits generate measurements of a constant sample area (Fig. 6). This does not necessarily mean that similar mineralogical interpretations cannot be obtained from different slit settings. Krylov *et al.*, 2008, obtained different values but identical smectite trends for the same samples analyzed at different laboratories using either fixed or adjustable slits. If the measurements are conducted at adjustable slit settings the XRD software converts the data to the XRD database format, for which fixed slit settings have been used.

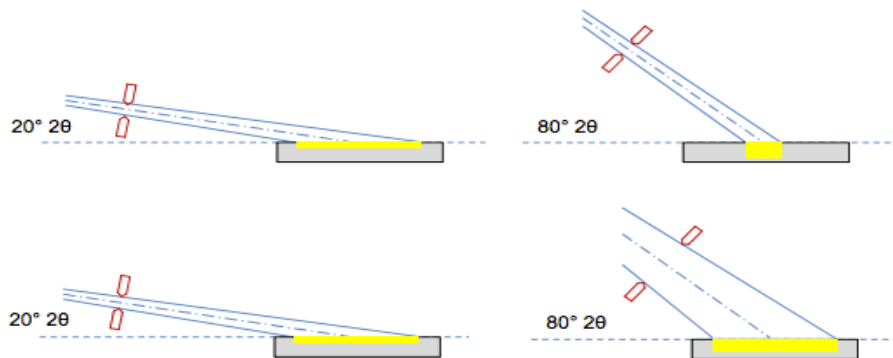


Figure 6. Constant irradiated sample volume at fixed slit settings (upper). Constant irradiated sample area at adjustable slit settings (lower) (RMS Foundation, 2013, <http://profex.doebelin.org/wp-content/uploads/2014/02/Lesson-2-Diffractometers-and-Phase-Identification.pdf>. Accessed 27 January 2015, modified in PowerPoint).

Five pure talc samples of the <2 μ m fraction and a pure quartz plate were measured with both a fixed width of 2° and adjustable widths, in order to evaluate whether or not it would lead to similar mineralogical interpretations. The remaining instrumental settings were the same as described in section 3.3.1. Figure 7 presents the average peak areas of the 3.34 Å quartz peak and the 9.33 Å, 4.68 Å and 3.12 Å talc peaks measured at the different slit settings. Table 1 and 2 present the individual sample data of the quartz peak respectively the talc peaks. The results show no differences between the slit settings for neither the quartz peak nor the talc peaks.

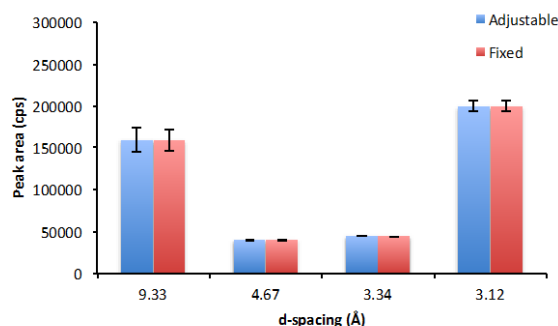


Figure 7. Average peak areas of the 3.34 Å quartz peak and the 9.33 Å, 4.68 Å and 3.12 Å talc peaks obtained at fixed and adjustable slit settings (n = 5). * indicates significant difference between the slit settings, bars = range.

Since the same quartz plate has been used the intensity variation of the 3.34 Å peak obtained from the five measurements reflects the variability of running the instrument, and has a range of ~ 740 cps and ~ 580 cps at adjustable respectively fixed slit settings.

Table 1. 3.34 Å peak area of five measurements of a quartz plate obtained at fixed and adjustable slit settings.

Sample	Peak area (cps)	
	3.34 Å	
	Fixed slit	Adjustable slit
Quartz plate	44293	44350
Quartz plate	44475	44789
Quartz plate	43900	44642
Quartz plate	44118	44046
Quartz plate	44138	44182

Since the same talc batch has been used the intensity variation of the talc peaks obtained from the five measurements reflects the amount of the sample displacement, which occurs when the sample is not on the focusing circle or in the center of the goniometer circle. Displacement from the focusing circle is caused by misalignment of the sample surface with the sample holder edge, and displacement from the goniometer circle is due to a not accurately centered sample on the filter and/or on the sample holder. Sample displacement is illustrated in Figure 8 and it is one of the greatest sources of error in most data and can lead to shifts in the peak positions and intensity variations due to asymmetric peak broadening. The intensity variation of the talc peaks may additionally be due to varying smoothness of the sample surfaces, since X-ray absorption due to unevenness can reduce peak intensities (Moore and Reynolds, 1997). The intensity variation of the talc peaks with adjustable slits show ranges of ~ 34200 cps (9.33 Å), ~2700 cps (4.68 Å) and ~ 16080 cps (3.12 Å). The intensity variation of the talc peaks with fixed slits show ranges of ~ 31750 cps (9.33 Å), ~2370 cps (4.68 Å) and ~ 16330 cps (3.12 Å).

Table 2. 9.33 Å, 4.67 Å and 3.12 Å peak areas of five talc samples of the <2µm fraction obtained at fixed and adjustable slit settings.

Sample	Peak area (cps)					
	9.33 Å		4.68 Å		3.12 Å	
	Fixed slit	Adjustable slit	Fixed slit	Adjustable slit	Fixed slit	Adjustable slit
Talc 1	169980	172355	40705	40502	205237	205649
Talc 2	158651	158634	39521	39764	201102	200262
Talc 3	154672	154860	39581	39427	207025	206210
Talc 4	139793	138711	38333	37806	190697	190132
Talc 5	171541	172914	39572	39415	194034	194802

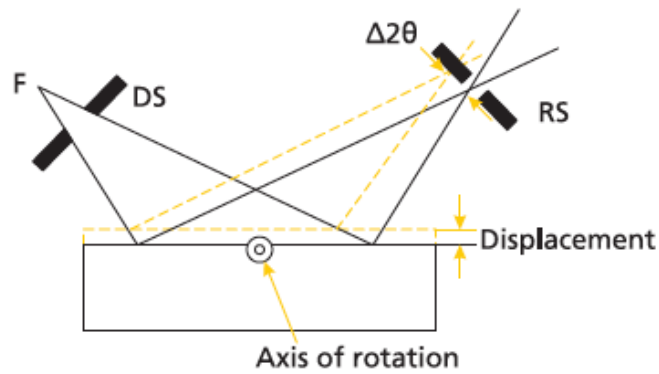


Figure 8. Sample displacement above the focusing circle (Ermrich and Opper, 2013, <http://www.panalytical.com/Technology-background/XRD-for-the-analyst-getting-acquainted-with-the-principles-booklet.htm>. Accessed 20 February, 2015).

3.6 Grain size analyses

Grain size analyses were performed with a Malvern Mastersizer 3000 laser particle analyzer at the Department of Geological sciences at Stockholm University. Enough sample mass to obtain obscuration between 5 and 20 % were first added to 50ml beakers containing deionized water and insonicated with an external ultrasonication bath before they were transferred into the dispersal unit. Deionized water with 3 ml 10 % $(\text{NaPO}_4)_6$ -solution was used as dispersion solution in order to obtain higher measurement precision. Parameter settings for further optimizing measurement precision were set as recommended by Granberg, 2012, which are presented in Appendix A, Table A1. Three replicates were made for both the 2-20 μm and <2 μm fraction of the upper and lower core section, yielding a total of 12 replicates, in order to determine the analytical precisions.

4. Results

4.1 1208A mineralogy and grain size

This study has determined the mineralogy and grain size of the <2 μm and 2-20 μm fraction in two core sections ~5-165 ka (0.2-7 mbsf) and ~2.27-2.91 Ma (107-133 mbsf) from Site 1208A on the central Shatsky Rise. Individual sample data are presented in Appendix B, Table B1-B4 and B6-B9. The weighting factors by Heath and Pisias, 1979, have been chosen for estimating the mineral proportions. The mineralogical compositions of the individual samples derived from the weighting factors by Biscaye and Corrected Biscaye can be found in Appendix B, Table B5 and B10.

The major mineral components of both size fractions are illite, kaolinite, chlorite, quartz and plagioclase. Smectite is also a significant component of the <2 μm fraction, but is either absent or present in lower amounts than the detection limit in the 2-20 μm fraction. The size fractions display overall significantly different ($\alpha = 0.05$) mineral proportions and peak area ratios. Primary minerals dominate the 2-20 μm fraction and clay minerals dominate the <2 μm fraction.

Table 3 presents the analytical precision of the major mineral components and grain size data obtained from replicates. The highest analytical precision of the minerals for both size fractions is shown by chlorite (<2 μm : 0.08 wt.%, 2-20 μm : 0.05 wt.%). The lowest analytical precision for the <2 μm and 2-20 μm fraction is shown by illite (1.38 wt.%), and plagioclase (0.75 wt.%) respectively.

Table 3. Analytical precision obtained from replicates

Parameter	Analytical precision	
	<2 μm	2-20 μm
Weight %		
Smectite	0.53	ND
Illite	1.38	0.33
Kaolinite	0.47	0.21
Chlorite	0.08	0.05
Quartz	0.36	0.50
Plagioclase	0.41	0.75
Unidentified	2.83	1.67
Grain size (μm)		
Mean	0.69	0.14
Median	0.07	0.05
Mode	0.01	0.11
Skewness*	1.53	0.08
Proportion (vol.%)		
Clay (<2 μm)	2.01	0.32
Silt (2-20 μm)	1.89	0.37
Sand (20-63 μm)	0.71	0.45

* unitless

4.1.1 Mineralogy

The normalized mineral peak areas of the <2 μ m and 2-20 μ m fraction in the upper and lower section are illustrated in Figure 9A and 9B. Notice the scale differences in the figures. The average mineral proportions are presented in Figure 10 and Table 4.

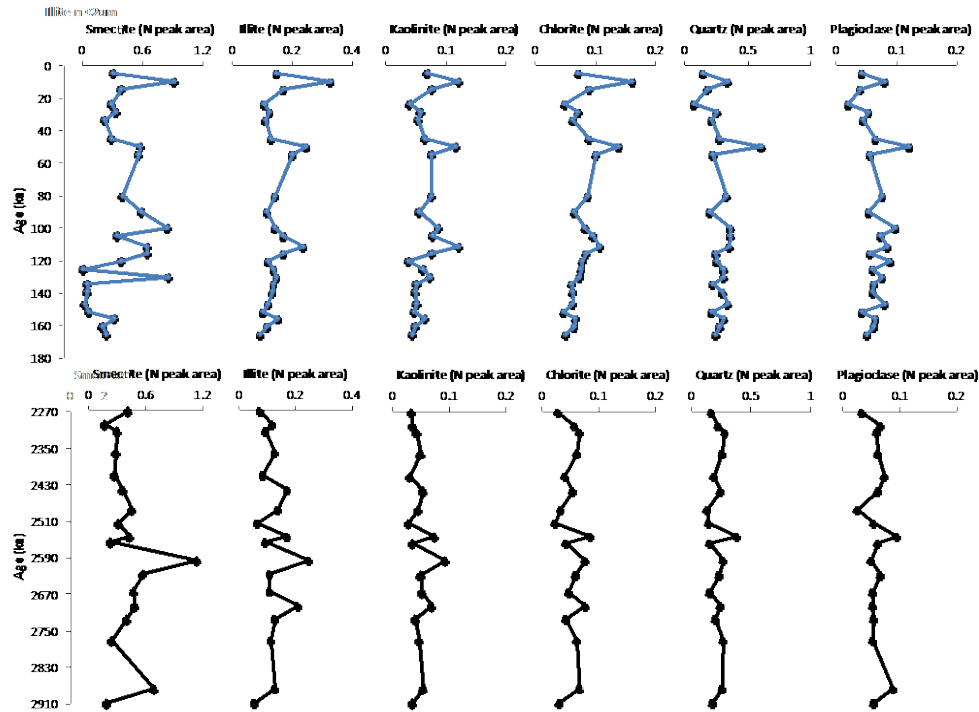


Figure 9A. Normalized peak areas of the <2 μ m fraction vs. age in the upper and lower section at 1208A.

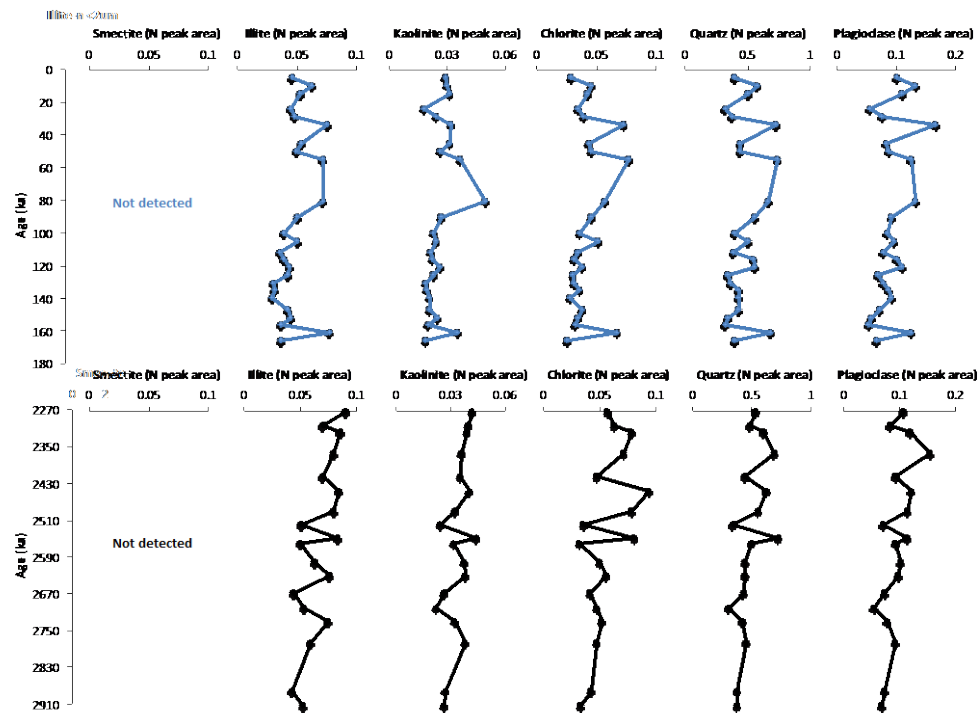


Figure 9B. Normalized peak areas of the 2-20 μ m fraction vs. age in the upper and lower section at 1208A.

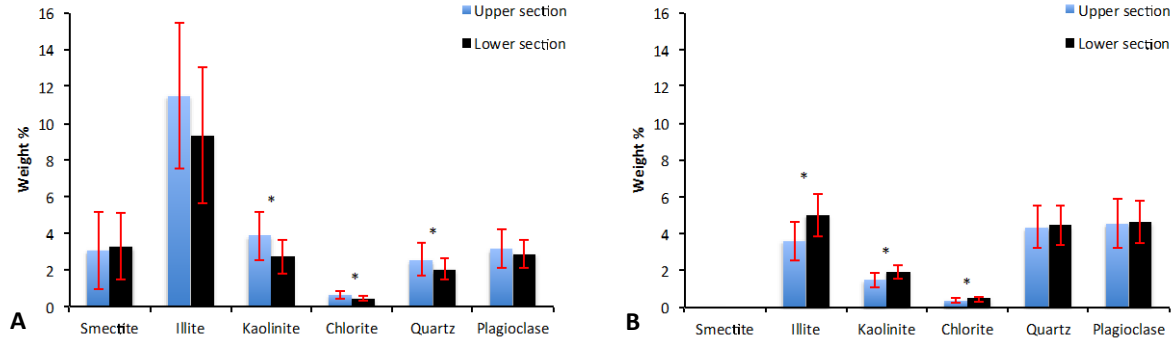


Figure 10. Average mineral proportions of the <2µm (A) and 2-20µm (B) fraction in the upper and lower section at 1208A. * indicates significant differences at $\alpha = 0.05$, bars = standard deviations.

Table 4. Average and range of the mineral proportions and peak area ratios in the <2µm and 2-20µm fraction in the upper and lower section at 1208A. Bold underlined data indicate significantly different averages between the sections at $\alpha = 0.05$. ND = not determined, (-) = no range.

Parameter	1208A mineralogy			
	<2µm		2-20µm	
	Upper section (n = 25)	Lower section (n = 18)	Upper section (n = 25)	Lower section (n = 18)
Weight %				
Smectite	3.1 (0.1-7.3)	3.3 (1.4-9.1)	ND	ND
Illite	11.5 (6.9-24.7)	9.3 (4.1-18.7)	<u>3.6</u> (2.2-5.8)	<u>5.0</u> (3.2-6.8)
Kaolinite	<u>3.9</u> (2.2-7.0)	<u>2.8</u> (2.0-5.3)	<u>1.5</u> (1.0-2.8)	<u>1.9</u> (1.3-2.5)
Chlorite	<u>0.7</u> (0.4-1.4)	<u>0.4</u> (0.2-0.7)	<u>0.4</u> (0.2-0.7)	<u>0.5</u> (0.3-0.8)
Quartz	<u>2.6</u> (0.7-5.6)	<u>2.0</u> (1.2-3.5)	4.4 (2.9-6.8)	4.4 (2.8-6.6)
Plagioclase	3.2 (1.0-5.9)	2.9 (1.3-4.6)	4.6 (2.6-8.1)	4.6 (2.6-7.5)
Unidentified	75.2 (52.6-85.1)	79.3 (61.4-87.9)	85.6 (77.1-90.2)	83.5 (77.5-88.9)
Peak area ratio				
K/C	0.9 (0.5-1.1)	0.9 (0.6-1.4)	0.6 (0.4-1.0)	0.6 (0.4-1.0)
K/I	0.4 (0.3-0.6)	0.4 (0.3-0.6)	0.5 (0.4-0.7)	0.5 (0.4-0.7)
S/I	<u>2.5</u> (0.1-6.0)	<u>3.4</u> (1.5-5.3)	ND	ND
C/I	<u>0.5</u> (0.4-0.7)	<u>0.4</u> (0.2-0.7)	0.9 (0.6-1.2)	0.8 (0.6-1.1)
Q/I	1.9 (0.7-2.8)	1.9 (0.9-3.2)	<u>10.1</u> (7.1-14.6)	<u>7.3</u> (5.5-10.1)
P/I	0.4 (0.2-0.7)	0.5 (0.2-1.0)	<u>2.0</u> (1.3-3.1)	<u>1.4</u> (1.0-1.9)
P/Q	0.2 (0.2-0.4)	0.3 (0.2-0.4)	0.2 (0.2-0.3)	0.2 (-)

The <2µm fraction shows the following order of decreasing mineral abundances: illite, kaolinite, plagioclase, smectite, quartz and chlorite in the upper section, and illite, smectite, kaolinite, plagioclase, quartz and chlorite in the lower section. The 2-20µm fraction shows the following order of decreasing mineral abundances: plagioclase, quartz, illite, kaolinite and chlorite in the upper section, and illite, plagioclase, quartz, kaolinite and chlorite in the lower section. Generally, the wt.% ranges in both fractions are wider in the upper than lower section. The mineral components display similar trends without any distinctive shifts for both the <2µm and 2-20µm fraction in the upper section. This is also observed for the minerals in the <2µm fraction in the lower section, with the exception of a pronounced smectite peak at ~ 2.6 Ma. The minerals in

the 2-20 μ m fraction show similar, slightly decreasing trends downcore in the lower section (Fig. 9).

No major differences in the mineral proportions or peak area ratios can be determined for either the <2 μ m or 2-20 μ m fraction between the upper and lower section, or at 2.6 Ma. However, some less pronounced changes can be observed. The <2 μ m fraction displays more kaolinite, chlorite and quartz, lower S/I and higher C/I peak area ratio in the upper than lower section. The 2-20 μ m fraction shows less illite, kaolinite and chlorite, and higher Q/I and P/I peak area ratio in the upper than lower section (Fig. 10 and Table 4).

The size range and mineral MARs have been estimated for the lower section. Due to unvarying trends and the limited data set, in which DBD values have been interpolated between few data points, no discussion regarding MARs will be provided in this study.

4.1.2 Grain size

The mean, median, mode, skewness and vol.% clay, silt and sand of the <2 μ m and 2-20 μ m fraction in the upper and lower section at Site 1208A are presented in Figure 11A and 11B, and average values are provided in Table 5. Notice the scale differences in the figures. The grain size distribution curves are illustrated in Figure 12.

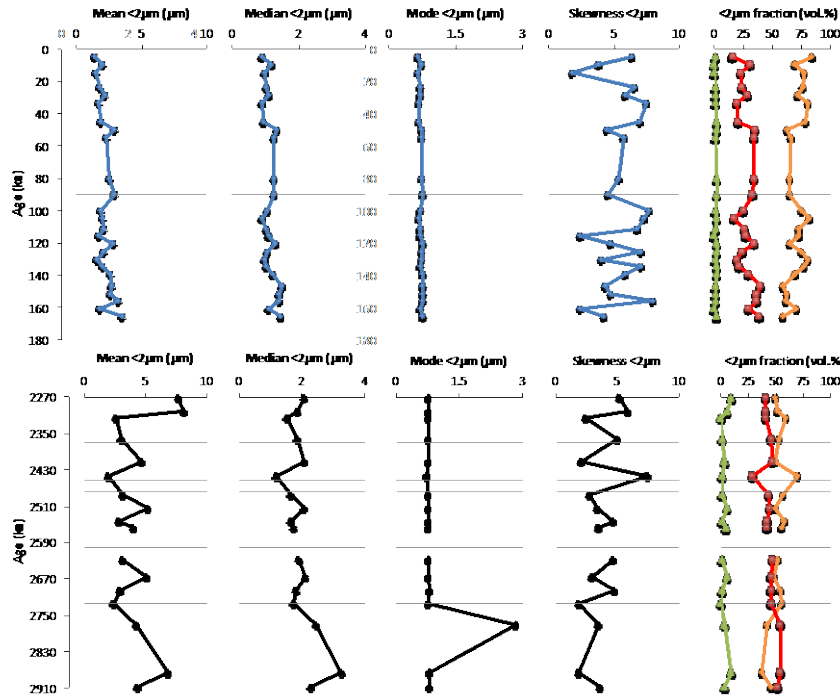


Figure 11A. Mean, median, mode, skewness and vol.% clay, silt and sand of the <2 μ m fraction vs. age in the upper and lower section at 1208A. Orange curve = clay (0-2 μ m), red curve = silt (2-20 μ m), green curve = sand (20-63 μ m), grey horizontal line = ash layer.

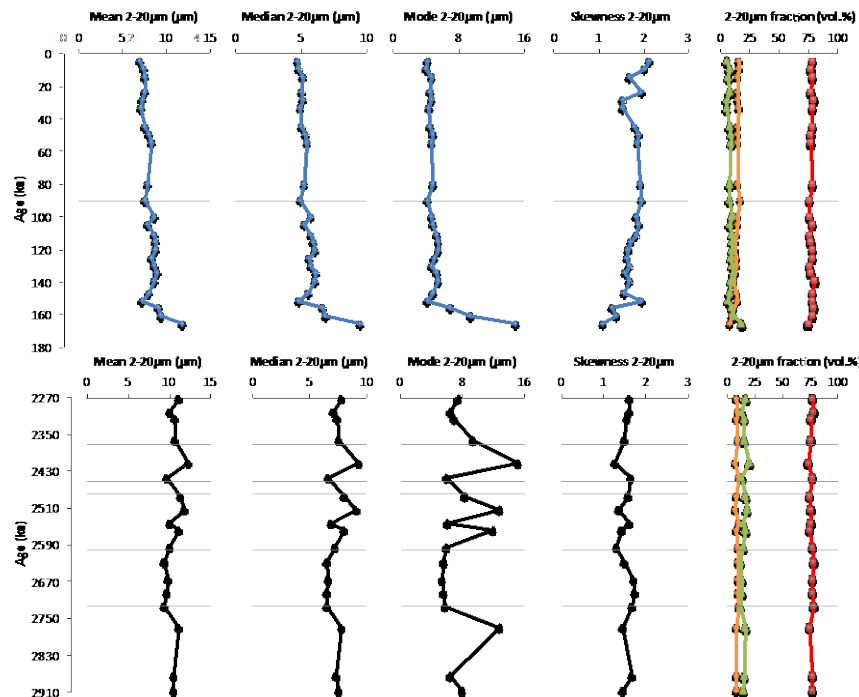


Figure 11B. Mean, median, mode, skewness and vol.% clay, silt and sand of the 2-20 μ m fraction vs. age in the upper and lower section at 1208A. Orange curve = clay (0-2 μ m), red curve = silt (2-20 μ m), green curve = sand (20-63 μ m), grey horizontal line = ash layer.

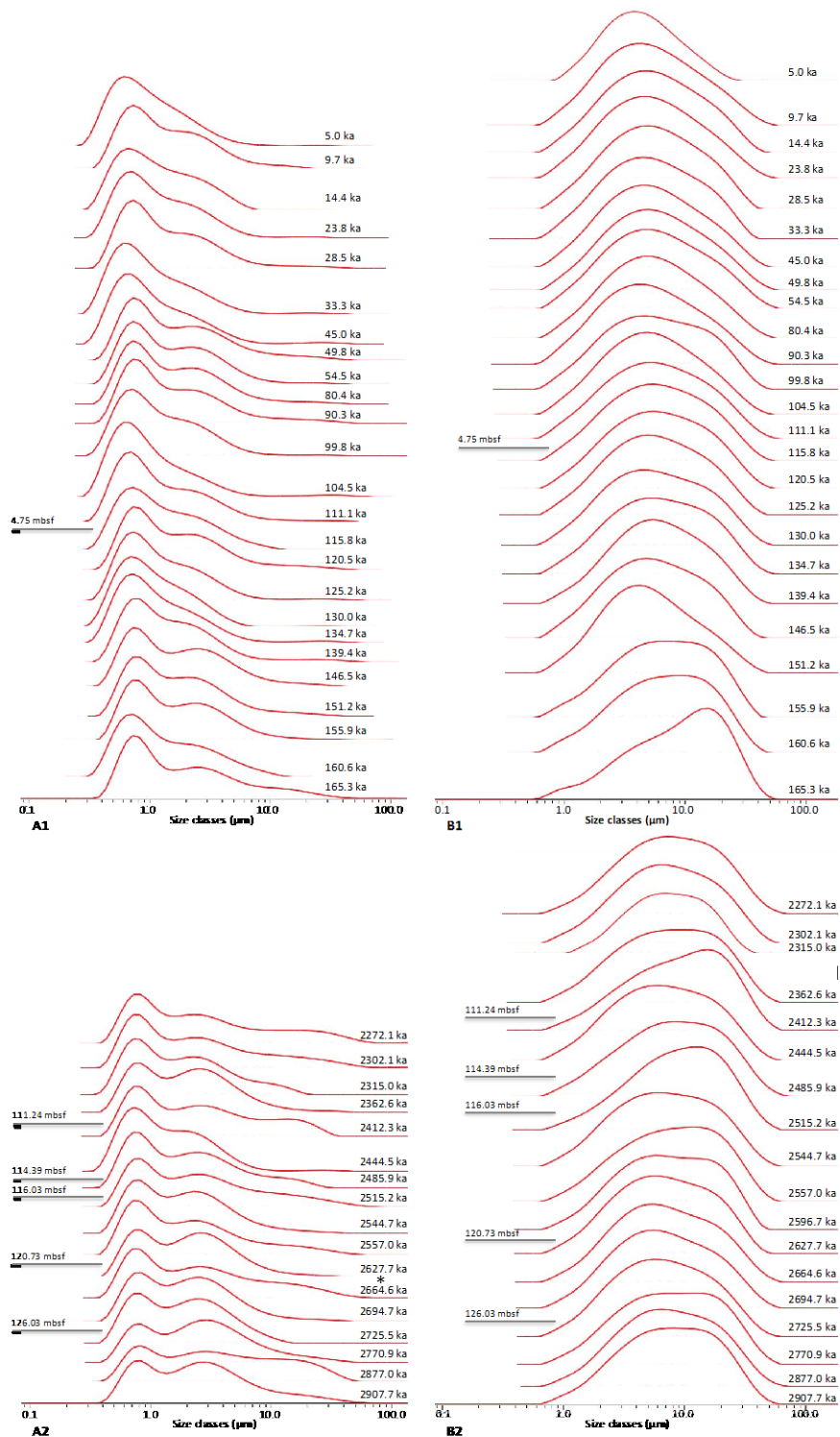


Figure 12. Grain size distribution curves of the <2µm (A) and 2-20µm fraction (B) in the upper (1) and lower (2) 1208A section. Grey horizontal line = ash layer, *= not enough <2µm material of sample 14H-2 10-12 left for analysis.

Table 5. Average grain size values and range of the <2 μ m and 2-20 μ m fraction in the upper and lower section at 1208A. Bold underlined data indicate significantly different averages between the sections at $\alpha = 0.05$.

Parameter	1208A grain size parameters			
	<2 μ m		2-20 μ m	
	Upper section (n = 24*)	Lower section (n = 18)	Upper section (n = 25)	Lower section (n = 18)
Grain size (μm)				
Mean	<u>2.2</u> (1.4-3.5)	<u>4.3</u> (2.0-8.1)	<u>8.2</u> (7.0-11.8)	<u>10.6</u> (9.4-12.3)
Median	<u>1.1</u> (0.9-1.5)	<u>2.0</u> (1.2-3.2)	<u>5.7</u> (4.7-9.5)	<u>7.5</u> (6.5-9.3)
Mode	0.7 (0.6-0.8)	0.9 (0.7-2.9)	<u>5.4</u> (4.1-15.0)	<u>8.1</u> (5.4-15.3)
Skewness**	<u>5.4</u> (1.7-8.1)	<u>3.9</u> (1.9-7.5)	<u>1.7</u> (1.1-2.1)	<u>1.5</u> (1.3-1.7)
Proportion (vol.%)				
Clay (<2 μ m)	<u>71.0</u> (58.8-83.9)	<u>51.8</u> (36.7-70.3)	<u>13.5</u> (7.5-16.5)	<u>8.8</u> (6.4-10.4)
Silt (2-20 μ m)	<u>27.8</u> (15.8-39.6)	<u>44.7</u> (28.9-54.6)	<u>77.8</u> (74.7-80.4)	<u>76.4</u> (72.9-78.5)
Sand (20-63 μ m)	<u>1.2</u> (0-2.4)	<u>3.4</u> (0-9.2)	<u>8.7</u> (5.5-17.8)	<u>14.9</u> (11.6-19.9)

* not enough <2 μ m material of sample 14H-2 10-12 left for analysis

** unitless

The <2 μ m fraction displays unvarying grain size trends throughout the entire upper section. The 2-20 μ m fraction shows uniform grain size trends down to ~ 151 ka, after which the mean, median and mode increase and the skewness decrease throughout the last part of the upper section (Fig 11A). The vol.% of clay and silt in the <2 μ m fraction average 71.0 % respectively 27.8%, and show opposite patterns with slight downcore variations. The vol.% of clay and silt in the 2-20 μ m fraction average 13.5 % respectively 77.8%, without downcore variation. The concentration of sand in the 2-20 μ m fraction starts to become higher than that of clay at 160.6 ka (Fig 11A).

The grain size trends are overall relatively uniform in both the <2 μ m and 2-20 μ m fraction in the lower section, with the exception of a distinctive mode peak in the <2 μ m fraction at ~2.77 Ma (Fig. 11A). The vol.% of clay and silt in the <2 μ m fraction average 51.5 % respectively 44.7 %, and show opposite patterns with slight downcore variation. The vol.% of clay is higher than of silt in the <2 μ m fraction down to ~2.73 Ma, after which the opposite relationship continues throughout the record. The vol. % of clay and silt in the 2-20 μ m fraction average 8.8 % respectively 76.4 %, and show no variation downcore. The vol.% of sand is slightly higher than of clay throughout the entire lower section in the 2-20 μ m fraction (Fig 11B).

The <2 μ m fraction generally shows bimodal strongly coarse skewed grain size distributions in both sections (Fig. 12A1, 12A2). The 2-20 μ m fraction shows overall unimodal grain size distributions in both sections, which are mainly slightly coarse skewed in the upper section and varies between slightly fine and coarse skewed in the lower section (Fig. 12B1, 12B2).

No major differences in the grain size parameters can generally be determined for either the <2 μ m or 2-20 μ m between the upper and lower section, or at ~2.6 Ma. The exceptions are shown by the vol.% clay and silt in the <2 μ m fraction, which are noticeably higher respectively lower in the upper than lower section. Some less pronounced differences can in general be observed in all grain size parameters between the upper and lower section (Table 5). The <2 μ m fraction displays smaller mean and

median, less sand, higher skewness value, and grain size distributions with generally larger differences between the major and minor modes in the upper than lower section. The 2-20 μm fraction shows smaller mean, median and mode, more clay and silt, less sand, and higher skewness value in the upper than lower section.

Some samples located closest to the ash layers have notably different appearances of their grain size distribution curves. For example, the differences between the finer major mode and coarser minor mode in the <2 μm fraction are particularly small for the samples at 2362.3 ka and 2627.7 ka, which are located above respectively below the ash layers at 111.24 and 120.73 mbsf (Fig. 12A2). However this is likewise observed for the three deepest samples in the <2 μm fraction, which are not located close to any identified ash layers. The 2-20 μm fraction of the sample at 2412.3 ka, which is located below the ash layer at 111.24 mbsf, has a particularly fine skewed grain size distribution (Fig. 12B2).

5. Discussion

The main variables that influence the eolian mineral assemblages in oceanic basins have briefly been presented in the introduction. This part of the discussion will initially be focused on the more comprehensive mineralogical and grain size effects induced by the influential paleoclimatic and volcanogenic factors. Even though it is complicated to interpret all variables that have affected the eolian fraction at 1208A, weathering conditions and mineralogy of the Asian source areas, transportation pathways and wind strength, contribution and alteration of volcanic material, and bioturbation will be discussed in further detail. The mineralogical and grain size results of the $<2\mu\text{m}$ and 2-20 μm fraction in the upper and lower section at 1208A will thereafter be addressed.

The next part of the discussion will first present background information regarding the earlier eolian studies and the compared samples, after which general influential factors for proxy record comparisons will be focused on. Lastly the results of the mineralogical comparisons will be presented and interpreted.

5.1 Paleoclimatic and volcanogenic factors

5.1.1 Weathering conditions and mineralogy of the Asian source areas

The temperature and humidity conditions in the source areas determine the dominant weathering processes. Chemical weathering predominates during hot and wet conditions and generally results in relatively higher formation clay minerals. Physical weathering predominates during cold and dry conditions and generally results in relatively higher formation of primary minerals (Chamley, 1989). However, physical and chemical weathering processes work in concert, and the accumulation of primary and clay minerals is therefore not restricted to solely either one of these weathering processes (Kasanin-Grubin, 2013).

The mineralogical composition of dust is also evidently dependent on the original mineral distribution of the underlying bedrock in the source areas. Wang *et al.*, 2012, concluded that the heterogeneous magnetic characteristics of the fine fraction in the surface sediments in the Ala Shan Gobi desert, a region displaying large dust emissions, are caused by the heterogeneous nature of the parent bedrock.

5.1.2 Transportation pathways and wind strength

The transportation pathways determine the transportation distance, and together with wind strength also the transportation time. Both these variables affect the degree of size and compositional fractionation and thus the relative proportions of the $<2\mu\text{m}$ and 2-20 μm fraction being delivered to the Shatsky Rise. Size and compositional fractionation during transportation also occurs within each size range. The $<2\mu\text{m}$ fraction retains substantially low settling velocity in the atmosphere, which results in long residence time and relatively low fractionation degree, as opposed to the 2-20 μm fraction (Blank *et al.*, 1985). These size differences would only cause mineralogical effects if the minerals were transported as individual grains, but due to the cohesive nature of $<10\mu\text{m}$ particles (Webb and Orr, 1997), they would likely also have been transported as larger aggregates.

The transportation pathways are also linked to the weathering conditions and mineralogy of the source areas since they determine which dust-producing regions potentially contribute to the dust load. For example, Xiao *et al.*, 2013, concluded that the

dominant source areas of fine grained dust deposited on the CLP have shifted as a result of changing wind patterns from southern Mongolia during glacial periods to northern China during interglacial periods. Despite its downwind location from the CLP long distance transportation to the Shatsky Rise may have resulted in compositional homogenization of the dust over larger areas, which could have limited the effects of glacial to interglacial fluctuations in dominant source areas.

5.1.3 Contribution and alteration of volcanic material

The volcanic arc systems that border the northern Pacific Ocean and lie beneath the prevailing westerlies can contribute substantial amounts of volcanic material to the seafloor and obscure the purely terrigenous dust records (Muhs, 2013; Patterson *et al.*, 1999). These volcanic systems can even provide higher dust amounts than what is supplied by the terrestrial source regions (Patterson *et al.*, 1999).

The terrigenous dust flux varies on orbital time scales, whereas the volcanic dust flux varies on tectonic time scales and can be considered as constant within the time periods investigated in this study. The influence of volcanic material is therefore relatively higher during periods of decreased terrigenous dust flux (Hovan *et al.*, 1991).

The presence of several volcanic ash layers at 1208A indicates that contribution of volcanic material may have significantly affected the mineralogy and grain size distribution. All of the petrographically analyzed ash layers deposited during the investigated time periods contain X-ray amorphous volcanic glass as main constituent, and plagioclase as main crystalline component (Gadley and Marsaglia, 2005).

Alteration of volcanic glass into saponite, which belongs to the smectite group, and X-ray amorphous allophane can occur in marine sediments during early diagenesis (White *et al.*, 2011; Chamley, 1989). Diagenic ash alteration at 1208A could be inferred by the presence of pyrite in the ash layers located at 4.75, 166.03 and 120.73 mbsf. Volcanic ash and its alteration products could therefore obscure the purely terrigenous signal and aggravate paleoclimatic interpretations when the mineralogy has been determined solely by XRD techniques.

5.1.4 Bioturbation

Bioturbation is a process dependent on a combination of local factors, such as current velocity, particulate organic carbon (POC) flux, oxygen level in the bottom waters and sediment column, and sedimentation rates (Smith and Rabouille, 2002). Bioturbation moves material up and down the sediment column, which can alter the chronostratigraphy. Burrowing organisms may also alter mineralogical composition through particle ingestion (Van Der Gaast, 1991). Seasonal changes in bioturbation are evident in marine sediments, with intensified activity and increased mixed layer depth observed during summer and autumn respectively (Teal *et al.*, 2008). Despite the obviously highly different environmental conditions for terrestrial and marine sediments, the ways in which they are reworked are similar and caused by equivalent behaviors such as lateral surface ploughing, burrowing, ingesting particles during scavenge, rolling and trampling (Meysman *et al.*, 2006). The extent of bioturbated sediments at 1208A during the investigated time periods is illustrated in Figure 14-16 in section 5.3, and in Figure A1-A6 in Appendix A.

5.2 1208A mineralogical and grain size interpretations

5.2.1 Mineralogy

The same mineral components have been identified in both size fractions, except for the absence of detectable smectite in the 2-20 μ m fraction. The <2 μ m fraction is relatively enriched in clay minerals and depleted in primary minerals compared to the 2-20 μ m fraction, and generally no corresponding mineralogical changes of the <2 μ m and 2-20 μ m have been observed. These results are consistent with the findings of previous studies, and can similarly conclude that mineralogical data obtained from one size fraction should not be used to characterize the entire mineralogical assemblage or interpret paleoclimatic conditions.

The unidentified component of both the <2 μ m and 2-20 μ m fraction is considerable, but Heath and Pisias, 1979, concluded that most of North Pacific sediments contain 20-50% of non-diffracting components, and that up to 70% of the sediments are not accounted for if one uses their weight conversion method. The 2-20 μ m fraction generally contains more unidentified material than the <2 μ m fraction, which could be a result of relatively higher proportions volcanic glass within the coarser size fraction. Further interpretations of the potential effects that volcanic glass could have induced on will be discussed in the following section.

No major mineralogical differences between the upper and lower section, or at ~ 2.6 Ma similar to Lingtai, could be determined in this study, which could be due to the relatively small number of samples within each section. Additionally, mineralogical variations caused by changing climatic conditions may have been obscured by the effects of large contribution of volcanic material, the generally moderate to common bioturbated nature of the sediments, and notable diagenetic alteration as indicated by the common presence of pyrite in various forms. The <2 μ m fraction of sample 14H-2 10-12 deposited at ~ 2.6 Ma does however show larger peak areas of smectite, illite and kaolinite, as well as amongst the largest peak areas of chlorite and quartz within the lower section (Appendix B, Table B6). This implies that higher sampling resolution around 2.6 Ma may facilitate the detection of more substantial mineralogical variations at 1208A in future studies.

Another possibility is that any major changes at 1208A caused by aridification of the Asian interior did not occur at the same time as those observed at Lingtai ~ 2.6 Ma. This could be supported by the findings by Arnold *et al.*, 1995, from Sites 885A/886B in the North Pacific, where an abrupt mineralogical change to an illite- and chlorite rich composition occurred at 3.8 Ma. The meteorological conditions in the late Pliocene resulted in reduced eolian deposition on the CLP compared to the early Pleistocene, even though the eolian source regions developed at that time. The lower elevation of the Tibetan Plateau generated predominantly west to east dust transportation from the desert regions, unlike the current northwesterly winds, and reduced air-mass subsidence over the CLP that limited eolian deposition. However, dust deposition in the North Pacific Ocean would not have been limited by these meteorological conditions (Arnold *et al.*, 1995). Extending the 1208A records in future studies could potentially reveal substantial mineralogical changes.

5.2.2 Grain size

The median grain size of eolian sediment is commonly used as a proxy for the strength of transporting wind systems, which is based on the fact that larger dust particles can be transported by stronger atmospheric circulation. The initially decreasing median of the 2-20 μm fraction in the upper section from 165.3 to 151.2 ka could be a result of weaker transporting wind systems. Extending the grain size record of the upper section is recommended for future studies in order to interpret whether an actual decreasing mode trend exists and can be attributed to decreasing wind strength.

Hovan *et al.*, 1991, initially encountered complications when interpreting the eolian grain size record from core V21-146 retrieved from Shatsky Rise, since coarser particles were deposited during interglacial rather than glacial periods and could therefore not directly be contributed to changes in wind strength. They determined through smear slide analyses that the volcanic particles were larger than the terrigenous particles, and concluded that the eolian grain size had been relatively more influenced by the coarser ash when reduced dust supply from the continents prevailed during interglacials.

Only one discrete ash layer is located in the upper section, as opposed to five in the lower section (Fig. 11 and 12). This may suggest that the smaller mean and median, larger clay and lower sand proportions, and higher skewness values of the <2 μm and 2-20 μm fractions in the upper than lower section have resulted from relatively lower ash contribution. More ash in the lower section could also explain the more pronounced second coarse mode of the <2 μm grain size distributions in the lower than upper section, and why the 2-20 μm grain size distributions varies between being slightly coarse and fine skewed in the lower section. The samples located closest to the ash layers have 1.1 μm larger average mean size and contain 2.1 vol.% less clay and 3.4 vol.% more sand in the 2-20 μm fraction than the remaining sample suite, which could support the interpretation of coarse ash influence. Numerous studies have been made on discrete ash layers in marine sediments, but only a few have investigated disseminated ash (White *et al.*, 2011; Huang, 1980; Scudder *et al.*, 2009). Huang, 1980, stated that dispersed ash is generally present in marine sediments in greater volumes than discrete ash layers. Influence of dispersed ash on the grain size record may be inferred by the lack of difference in the remaining grain size parameters, and the neither consistently nor exclusively deviating appearances of the distribution curves of the samples closest to the ash layers. This could be supported by the random or weak linear relationships between median and the different mineral proportions, and the considerable concentration of unidentified material of both size fractions, which could partially be composed of disseminated X-ray amorphous volcanic glass or allophone.

Another potential explanation for the observed grain size differences between the upper and lower section could be that the former has been processed for opal removal. However, no significant differences in unidentified material between the sections could be determined for either size fraction, and no broad humps were evident in the diffractograms at $\sim 4.1 \text{ \AA}$. The observed grain size differences therefore seem unlikely to have been caused by differences in opal contents.

The purely eolian bulk fraction of North Pacific sediments from the Asian sources has a unimodal grain size distribution (Rea and Hovan, 1995; Sun *et al.*, 2002). Future studies could therefore benefit from conducting additional grain size analyses on the eolian bulk fraction, and complementing smear slide analyses in order to further evaluate the influence of ash on the grain size, as well as on the mineralogical, record from Site 1208A.

5.3 Comparative settings

The relevant samples for each mineralogical comparison will be presented in this section, as well as general information about the sites and dust cruises, which locations are illustrated in Figure 13. Two separate figures present the samples of the Lingtai and Sites 885A/886B comparisons each, Figure 14 and 15 respectively 16 and 17, due to the extensive time gap between the upper and lower 1208A sections. In order to conduct the mineralogical comparisons all data records have been converted to weight % by using the weighting factors by Heath and Pisias, with consideration to the possibility that they are not equally suitable for all records. The mineral proportions have subsequently been normalized to 100 wt.% to exclude the undetermined components from the comparisons.

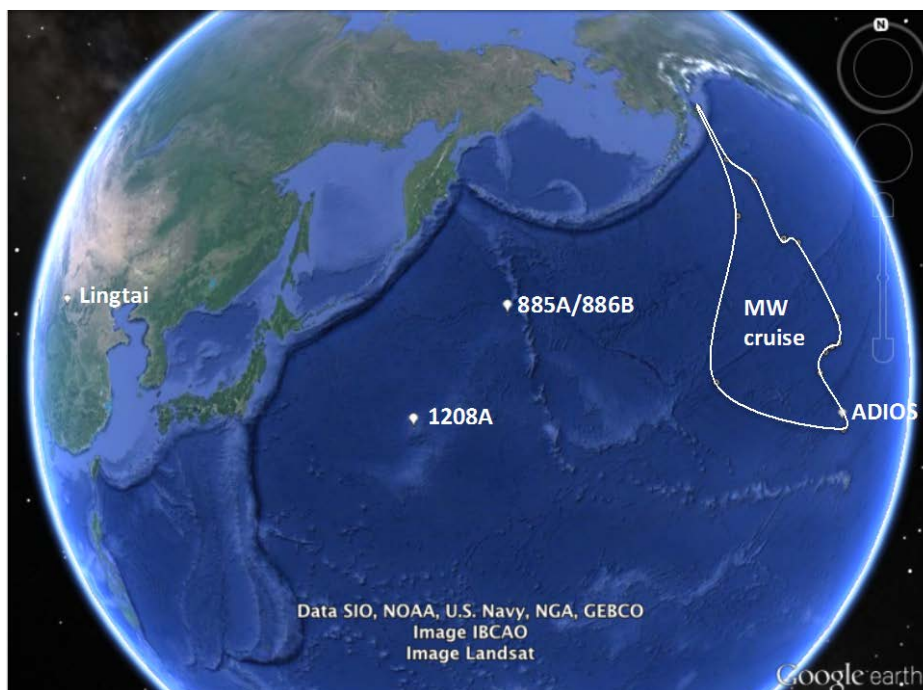


Figure 13. Map displaying the locations of the comparing sites/sampling stations (generated 26 January, 2105, in Google Earth version 7.1.2.2041).

The Lingtai section is located in the central part of the CLP, 107°30'33"E, 35°00'75"N (Fig. 13), at approximately 1340 m above sea level. It is amongst the oldest and most intact sections currently found on the plateau. The annual mean temperature and precipitation are 9.1°C respectively 600 mm, which is typical for the present warm and humid climate at the CLP (Ding and Yang, 2000). The Lingtai samples are from the Holocene soil, Malan Loess, Upper Lishi and Wucheng lithostratigraphic units and the red clay deposit, and have been grouped into paleosoil (n = 10), loess (n = 45) and red clay (n = 6) units. These will be compared to 1208A units composed of samples that corresponds to the depositional time of paleosoil (n = 14), loess (n = 22) and red clay (n = 7) at Lingtai (Fig. 14 and 15). This particular comparison is based only on the average mineralogical composition of the <2µm fraction.

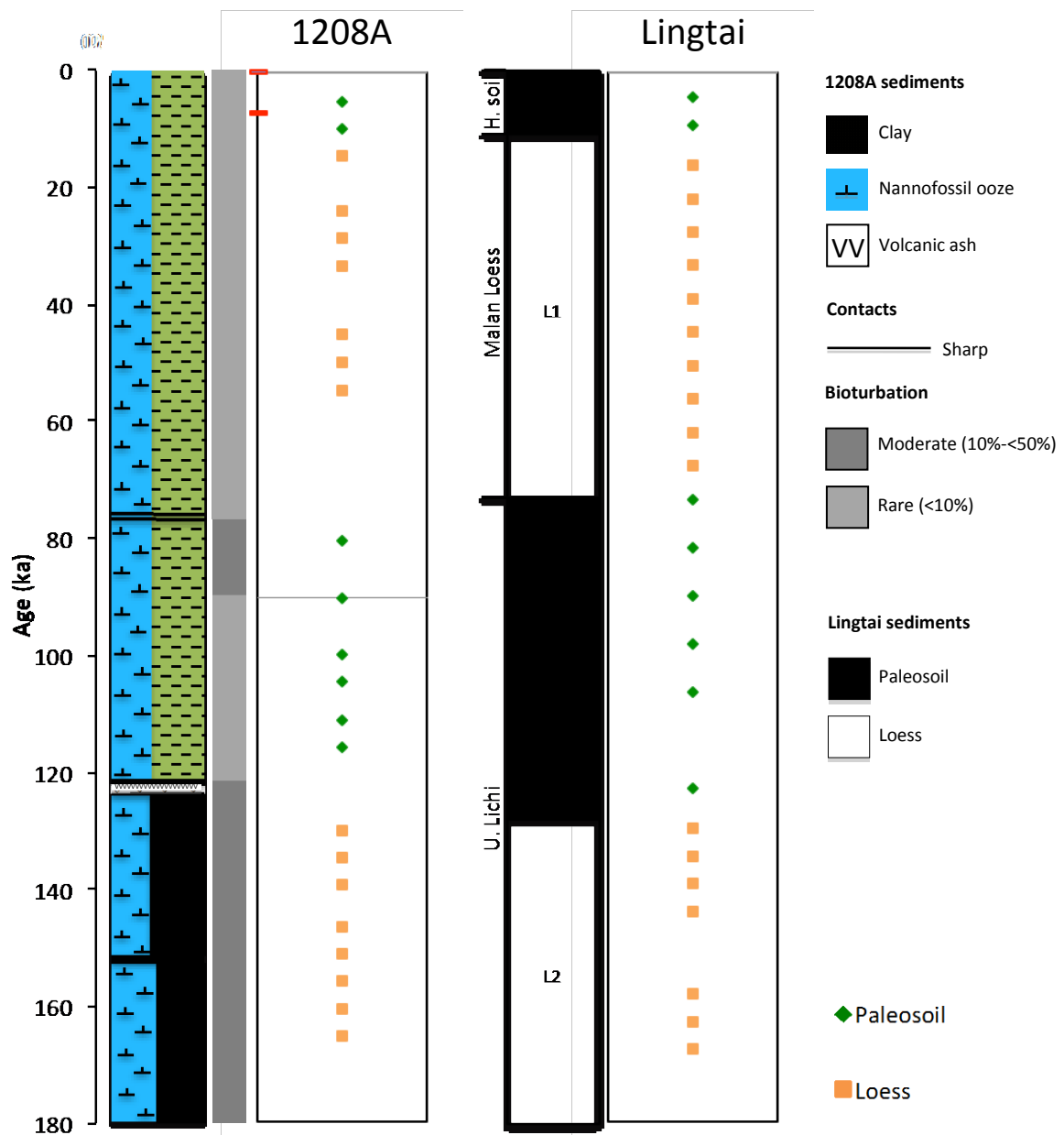


Figure 14. Compared paleosoil and loess samples from the Holocene soil, Malan loess and Upper Lichi lithostratigraphic units at Lingtai and approximate age corresponding samples from the upper section at Site 1208A vs. age. Red line = age datum, grey horizontal line = ash layer. Geomagnetic ages of the ash layers by Gadley and Marsaglia, 2005. The lithology and bioturbation columns for 1208A are based on the ODP visual core descriptions by the Shipboard Scientific Party, 2002, and the lithology column for Lingtai is based on Figure 3 in Gylesjö and Arnold, 2006.

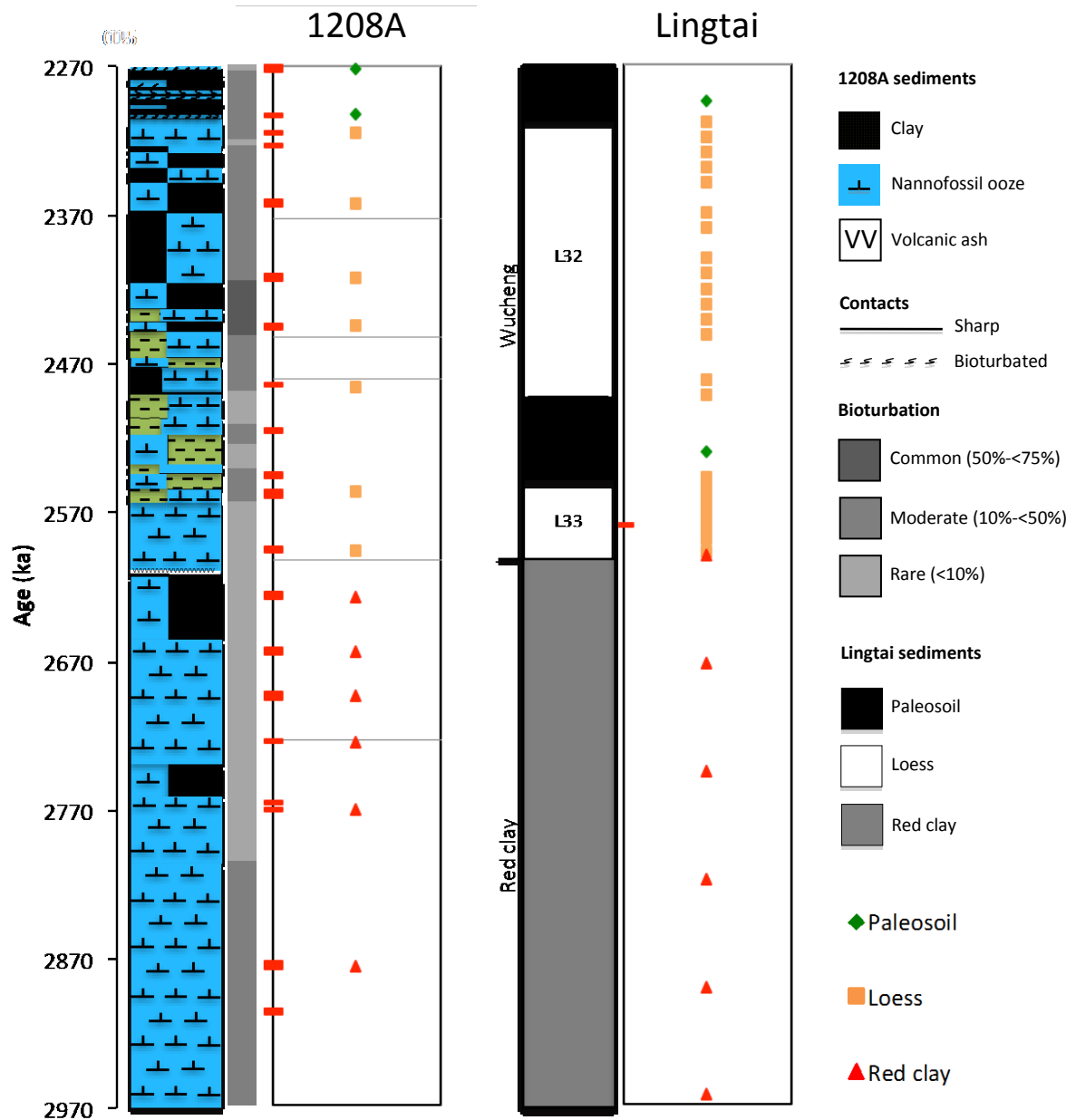


Figure 15. Compared paleosol, loess and red clay samples from the Wucheng and red clay lithostratigraphic units at Lingtai and approximate age corresponding samples from the lower section at 1208A vs. age. Red line = age datum, grey horizontal line = ash layer. Geomagnetic ages of the ash layers by Gadley and Marsaglia, 2005. The lithology and bioturbation columns for 1208A are based on the ODP visual core descriptions by the Shipboard Scientific Party, 2002, and the lithology column for Lingtai is based on Figure 3 in Gylesjö and Arnold, 2006.

The dust samples were obtained during the 1986 Moana Wave (MW) SEAREX expedition from Hawaii to Alaska, and the 1987 ADIOS cruise from Hawaii to a sampling station located at 26°N 155°W (Fig. 13). All samples were collected with paired 1m² nylon meshes during rain-free periods of the springtime maximum dust flux (Arnold *et al.*, 1998). The dust assemblages are represented by 10 samples from each cruise, and the surficial 1208A sediments are represented by the three samples deposited over the last 14.4 ka. This comparison is based on the average mineralogical composition of the <2µm and 2-20µm fraction.

Sites 885A and 886B are located at 44°41'N, 168°16'E and 44°41'N, 168°14'E respectively in the North Pacific Ocean (Fig. 13) at a water depth of approximately 5700 m. The sites were drilled during the 1993 ODP Leg 145 expedition and contain three stratigraphic sedimentary units. A composite depth model for 885A/886B has been developed by Dickens *et al.*, 1995. The Pliocene to late Pleistocene Unit I (0-23.5 mcd) is of interest to this comparison, which has a reddish brown to brown clay composition. Due to the limited number of 885A and 886B samples with corresponding ages to the 1208A samples the entire data sets of sedimentary Unit 1 from 885A (n = 17), and 886B (n = 17) have been combined and compared to the whole data set from 1208A (n = 43) (Fig. 16 and 17). This comparison is based on the average mineralogical composition of the <2µm and 2-20µm fraction.

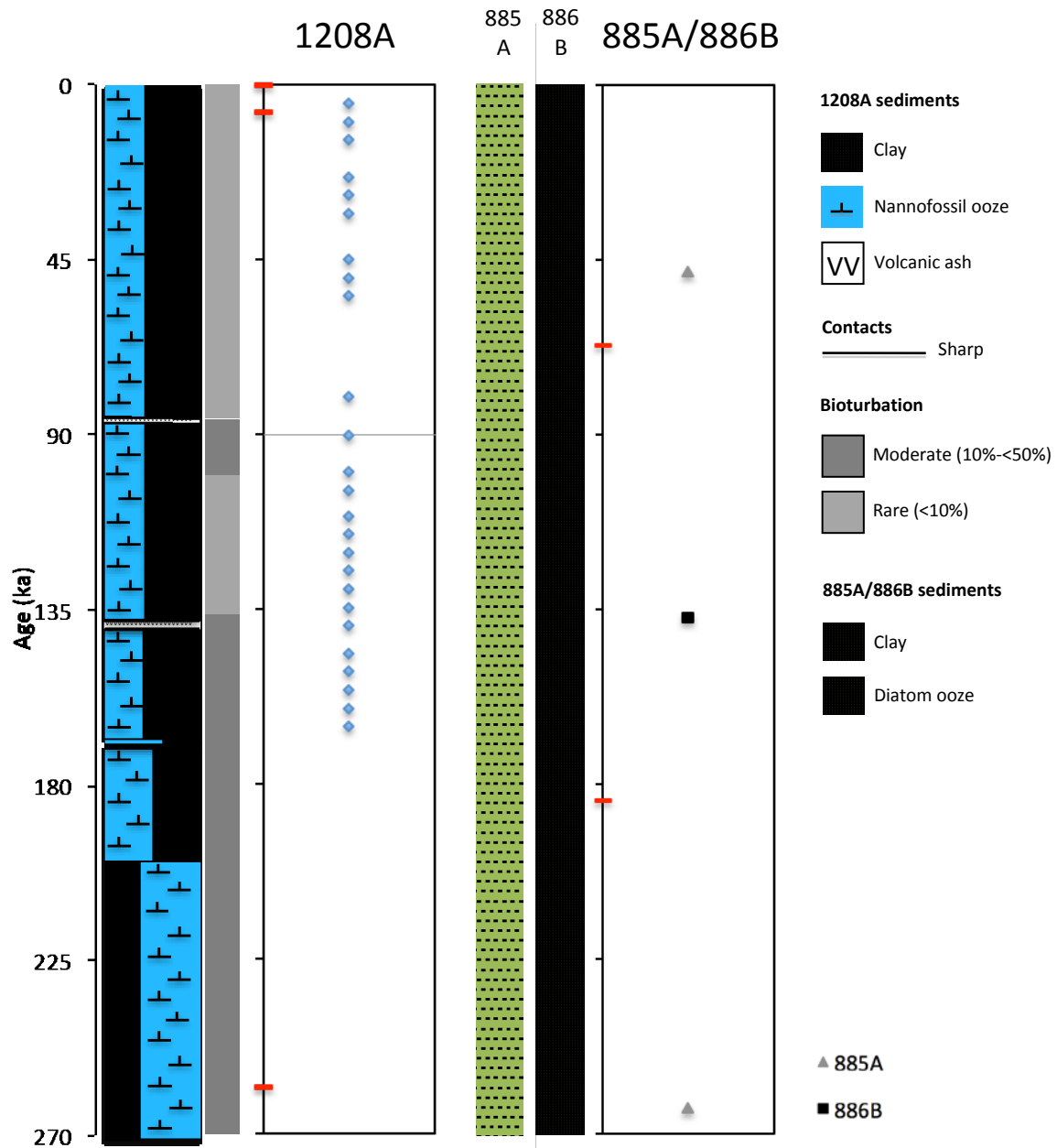


Figure 16. Compared samples from the upper part of Unit 1 at Sites 885A/886B, and from the upper section at Site 1208A vs. age. Red line = age datum, grey horizontal line = ash layer. Geomagnetic ages of the ash layers by Gadley and Marsaglia, 2005. The lithology and bioturbation columns for 1208A are based on the ODP visual core descriptions by the Shipboard Scientific Party, 2002, and the lithology columns for Sites 885A/886B are based on the ODP visual core descriptions by the Shipboard Scientific Party, 1993.

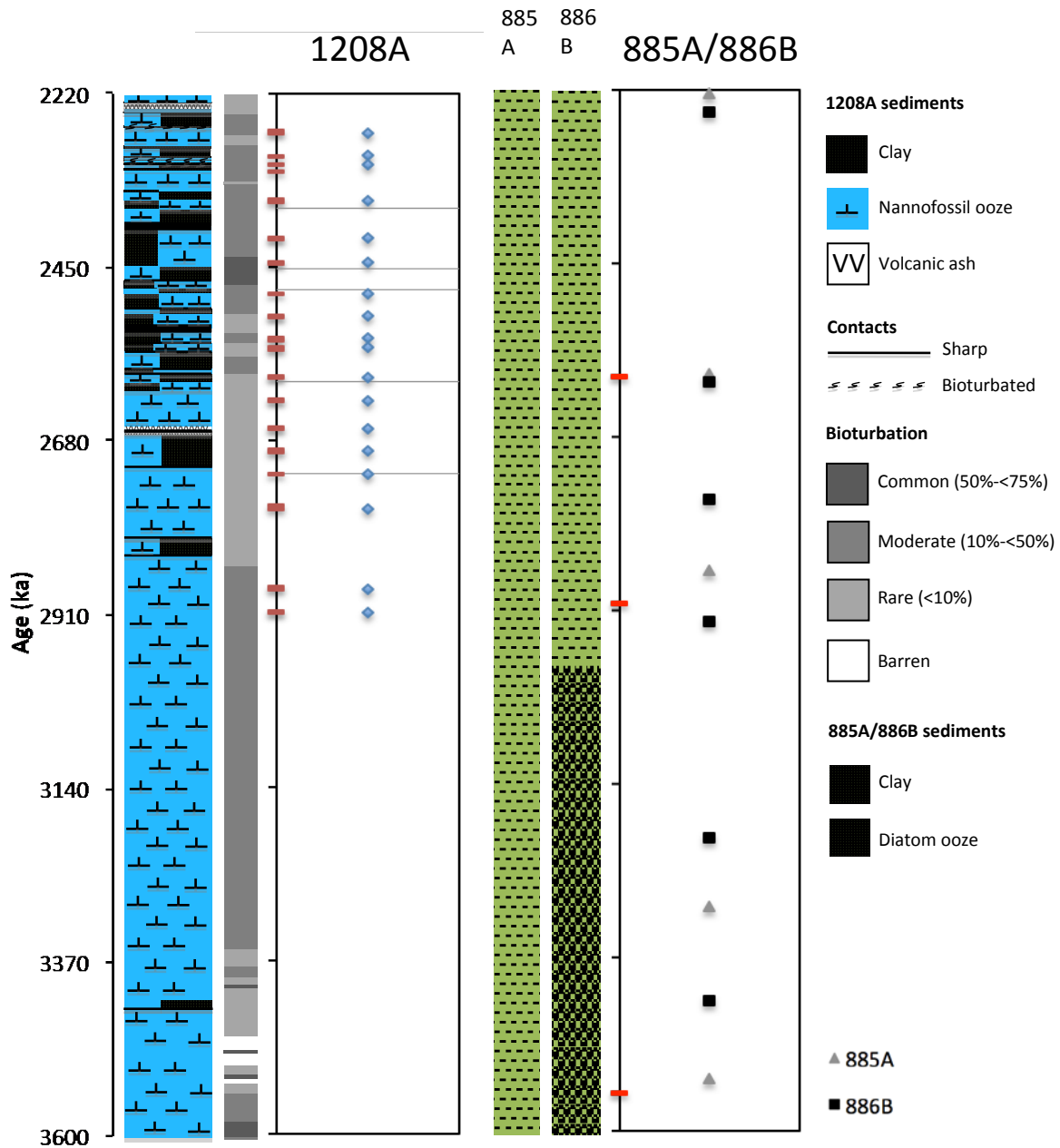


Figure 17. Compared samples from the lower part of Unit 1 at Sites 885A/886B, and from the lower section at Site 1208A vs. age. Red line = age datum, grey horizontal line = ash layer. Geomagnetic ages of the ash layers by Gadley and Marsaglia, 2005. The lithology and bioturbation columns for 1208A are based on the ODP visual core descriptions by the Shipboard Scientific Party, 2002, and the lithology columns for Sites 885A/886B are based on the ODP visual core descriptions by the Shipboard Scientific Party, 1993.

5.4 General influential factors for proxy record comparisons

The advantage of this study is the use of the same comparative proxy that facilitates direct comparisons between the sites. Every proxy has been influenced by a distinctive configuration of factors such as environmental conditions and climatic thresholds (Blauuw, 2012), and using the same proxy therefore avoids these complications. However, one must consider the effects of other influential factors such as age model, resolution, laboratory and analytical techniques in order to interpret similarities and differences between climatic records in the present and in the geological past. The objective of this section is to identify and discuss these factors, but their specific influences will not be addressed in the following comparisons.

5.4.1 Age models and resolution

It is crucial to attain an accurate age model in order to gain significant information regarding climatic proxies and compare them to global or regional climatic records. Many dating techniques have been used to develop age models for climatic archives, and all have unavoidably inbuilt uncertainties which must be considered when interpreting any proxy record in order to interpret whether observed variations depend on actual differences in the proxy data or not. Logically, the number of dating points and their concomitant uncertainties determine the age model quality, but only a few actual dating points are generally obtained due to for instance sparse sample material, time constraints and expensive analytical techniques (Breitenbach *et al.*, 2012). Paleomagnetic reversal stratigraphy has been used to develop the age model for Lingtai, and some sections have been tuned to orbital parameters. The age models for 885A/886B and the upper 1208A section are derived from paleomagnetic reversal stratigraphy and biostratigraphy. The age model for the lower 1208A section has been developed from δO^{18} stratigraphy, which age-depth relationship is illustrated in Figure 18.

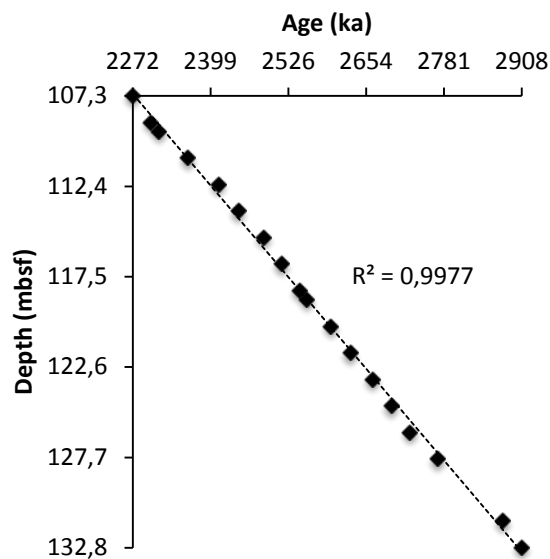


Figure 18. Age-depth relationship of the lower 1208A section.

The age datums for the relevant core sequences from Lingtai, Sites 885A/886B and the upper 1208A section are presented in Table B11-B14 Appendix B. The entire sets of age datums can be found in Ding *et al.*, 1999 for Lingtai, in Dickens *et al.*, 1995 for 885A/886B and in Evans, 2006, Bown 2005 and Venti and Billups, 2012 for 1208A. If similar origin of the eolian sediments from 1208A and Lingtai can be inferred by using mineralogy as direct comparative proxy, it would enable linkage of the Lingtai sequence to the well-established marine $\delta^{18}\text{O}$ timescale, such as Hovan *et al.*, 1989, succeeded with for the Xifeng loess-soil sequence, but without the complications of comparing different proxy types.

High frequency climatic variations will not be attained if the age resolution is not sufficiently high, but obtaining large sample suites and developing high-resolution records may be impeded by low sediment accumulation rates, besides the economical and time aspects. The average linear sedimentation rate of the loess-paleosol sequence and red clay sequence at Lingtai have been calculated to approximately 6.73 cm/kyr respectively 2.98 cm/kyr (Ding *et al.*, 1999). Equal average linear sedimentation rates of 0.46 cm/kyr in Unit I at 885A and 886B have been inferred through comparisons of depth intervals between susceptibility datums (Arnold *et al.*, 1995). Age range, resolution and number of samples of the compared sections are presented in Table 6.

Table 6. Age range, resolution and sample number of the units for each comparison

	Age range (ka)	Age resolution (cm/k.y.)	Nr of samples
1208A-Lingtai			
Paleosol			
1208A	5.0-2544.7	4.4	14
Lingtai	4.3-2531.1	7.1	10
Loess			
1208A	14.4-2596.7	4.2	22
Lingtai	16.0-2598.3	8.9	45
Red clay			
1208A	2627.7-2907.7	4.2	7
Lingtai	2600.7-2963.9	4.1	6
1208A-MW/ADIOS			
1208A	5.0-14.4		3
MW	current	-	10
ADIOS	current	-	10
1208A-885/886B			
1208A	5.0-2907.7	23.9	43
885A	48.0-3532.2	175.3	17
886B	137.1-3428.3	161.2	17

5.4.2 Laboratory techniques

Sample preparation procedures must generate as low as possible chemical and physical degradation of the fragile clay particles for mineralogical studies by XRD techniques (Moore and Reynolds, 1997). Carbonates, iron oxides and biogenic silica are common constituents of marine sediments, which will contribute to the diffraction pattern unless they are removed during the pre-treatment procedures. Iron oxides occur not just as discrete phases in sediments but may also form surface coatings on the clay minerals (Varadachari *et al.*, 2006). However, pre-treatments involving acids for especially iron oxide and biogenic silica removal can cause reduced degree of crystallinity through structural degradation and result in decreased peak intensities of the remaining mineral components (Panda *et al.*, 2010). Neither have the removal procedures, diffractometer models nor XRD slit types been the same in the comparing studies (Table 7), which could induce dissimilarities between the records.

Table 7. Removal procedures, diffractometer and XRD slit type used in the comparative studies.

	Removals	Diffractometer	XRD slit type
1208A upper section	Carbonate, iron oxide, opal	PANalytical X'Pert Powder	Adjustable
1208A lower section	Carbonate	PANalytical X'Pert Powder	Adjustable
Lingtai	Carbonate, iron oxide	Philips PW 1730 series	Fixed
MW/ADIOS	None	Scintag diffractometer	Fixed
885A/886B	Iron oxide, opal	Scintag diffractometer	Fixed

5.4.3 Analytical techniques

The results of mineralogical studies can be greatly affected by analytical inconsistencies regarding peak area determination (Moore and Reynolds, 1997; Vogt, 2009). Automatic peak area determination is not recommended for single peak clay mineral analyzes since they exhibit too high chemical and structural variability for these procedures to be accurately determined. XRD analyzes therefore require a certain degree of subjectivity, which makes it ideally to have a single analyst (Vogt, 2009).

Analytical inconsistency also concerns the single analyst, whom has to determine the peak areas consistently throughout the entire sample suite. In order to evaluate my ability to determine the peak areas in a consistent manner I reanalyzed the 9.9 Å illite peak and the combined 14Å chlorite and smectite peak of the <2µm for all samples from the upper 1208A section. Illite was chosen since it generally displayed sharp peaks even

in the <2 μ m fraction, and the combined 14Å peak was chosen since semi-quantitative estimations of smectite can be problematic due to its tendency to generate especially broad peaks of low intensities (Singh and Agrawal, 2012), which is consistent with the characteristics observed in the diffractograms from this study. A fair range of my analytical consistency could therefore be provided by reanalyzes of these peaks. The peak areas obtained from two analyses series are presented in Figure 19. Significant differences were observed for the average 14 Å peak area but not for the average illite peak area. However, the trends from the two analysis series remained essentially the same for both peaks.

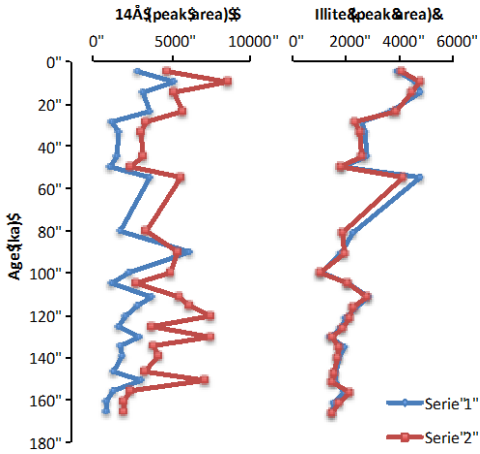


Fig 19. Two analyses series of the 14 Å combined smectite and chlorite peak area and the 9.9 Å illite peak area

5.5 Mineralogical comparison between 1208A and previous eolian studies

This final part of the discussion will present the comparative mineralogical data and focus on how most of the indicated differences can be explained by transportation time and distance from the main Asian source areas, volcanic contribution and incorporation of dust from other source regions. The results are illustrated in Figure 20 and Table 8 for the Lingtai comparison, in Figure 21, 22 and Table 9 for the MW/ADIOS comparison, and lastly in Figure 23 and Table 10 for the 885A/886B comparison. The results are presented separately but will be discussed together.

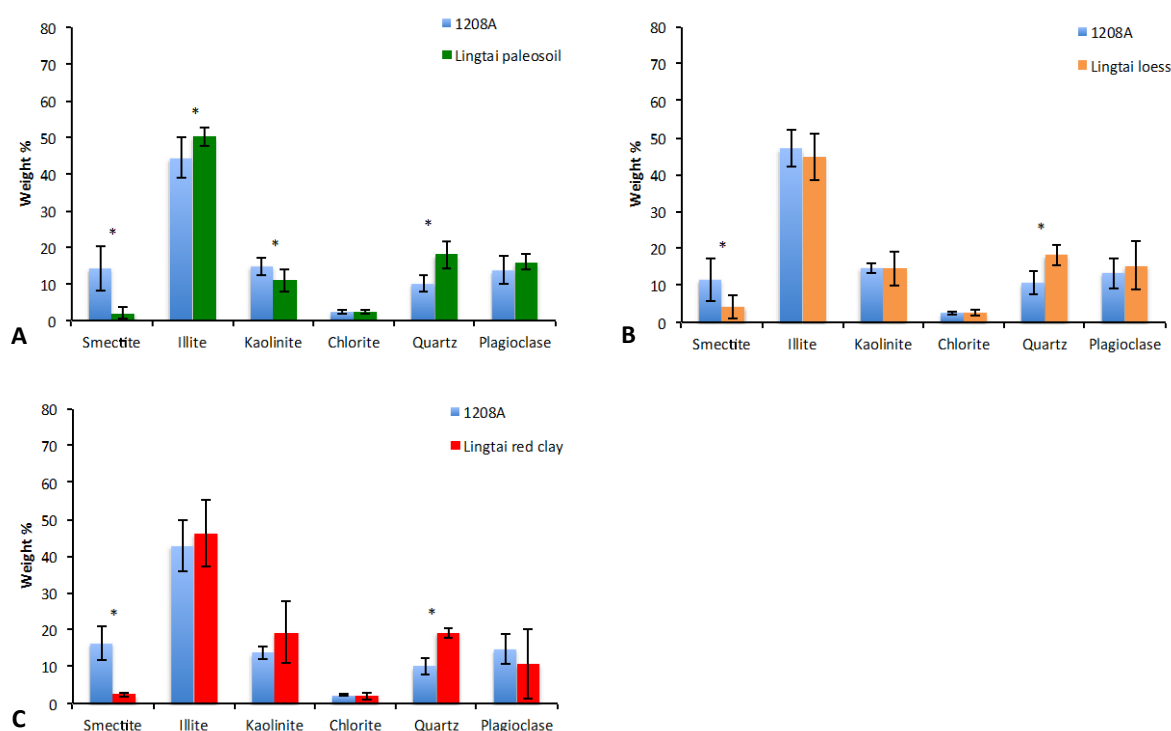


Figure 20. Average mineralogical composition of the <2µm fraction of (A) 1208A (n = 14) and Lingtai soil (n = 10), (B) 1208A (n = 22) and Lingtai loess (n = 45), and (C) 1208A (n = 7) and Lingtai red clay (n = 6) compared in this study. * indicates significant differences at $\alpha = 0.05$, bars = standard deviation.

Table 8. Average wt.% of the main mineral components within Lingtai paleosoil, loess and red clay and age corresponding samples at 1208A. Bold underlined data indicate significant differences between the units at $\alpha = 0.05$.

Mineral	Average weight %					
	1208A (n = 14)	Lingtai paleosoil (n = 10)	1208A (n = 22)	Lingtai loess (n = 45)	1208A (n = 7)	Lingtai red clay (n = 6)
Smectite	<u>14.3</u>	<u>2.1</u>	<u>11.5</u>	<u>4.3</u>	<u>16.3</u>	<u>2.3</u>
Illite	<u>44.4</u>	<u>50.3</u>	47.1	44.8	42.8	46.2
Kaolinite	<u>14.9</u>	<u>11.2</u>	14.7	14.6	13.8	19.4
Chlorite	2.5	2.4	2.6	2.7	2.2	2.1
Quartz	<u>10.1</u>	<u>18.0</u>	<u>10.7</u>	<u>18.2</u>	<u>10.1</u>	<u>19.3</u>
Plagioclase	13.8	16.1	13.4	15.4	14.7	10.8

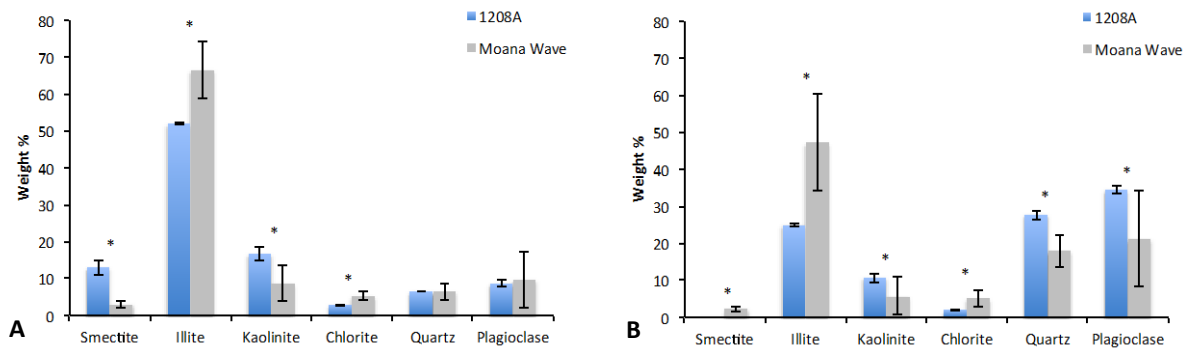


Figure 21. Average mineralogical composition of the (A) <2µm and (B) 2-20µm fraction of Moana Wave dust (n = 10) and surficial 1208A sediments (n = 3). * indicates significant differences at $\alpha = 0.05$, bars = standard deviation.

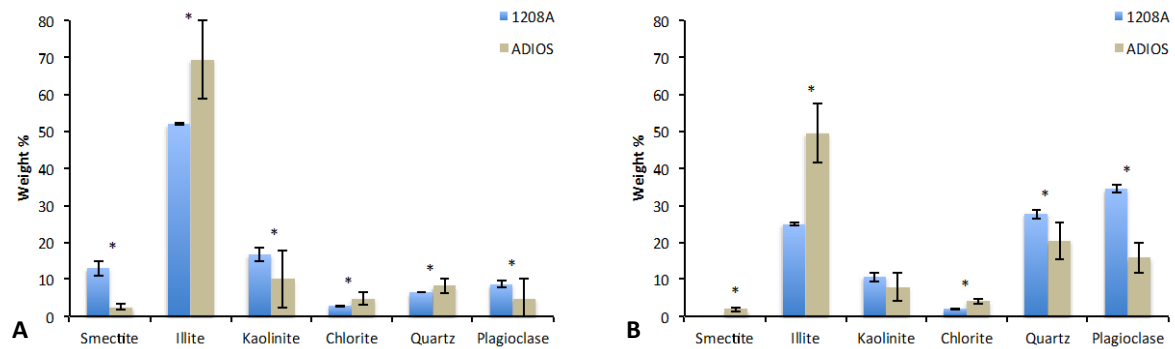


Figure 22. Average mineralogical composition of the (A) <2µm and (B) 2-20µm fraction of ADIOS dust (n = 10) and surficial 1208A sediments (n = 3). * indicates significant differences at $\alpha = 0.05$, bars = standard deviation.

Table 9. Average weight % of the main mineral components of the <2µm and 2-20µm fraction in surficial sediments at 1208A and mineral dust collected over the North Pacific Ocean during the Moana Wave and ADIOS cruises. Bold underlined data indicate significant differences between 1208A and each dust cruise at $\alpha = 0.05$. ND = not determined.

Mineral	Average weight %							
	<2µm				2-20µm			
	1208A (n = 3)	MW (n = 10)	1208A (n = 3)	ADIOS (n = 10)	1208A (n = 3)	MW (n = 10)	1208A (n = 3)	ADIOS (n = 10)
Smectite	<u>13.1</u>	<u>3.1</u>	<u>13.1</u>	<u>2.5</u>	ND	<u>2.4</u>	ND	<u>2.0</u>
Illite	<u>52.0</u>	<u>66.5</u>	<u>52.0</u>	<u>69.5</u>	<u>25.0</u>	<u>47.3</u>	<u>25.0</u>	<u>49.5</u>
Kaolinite	<u>16.7</u>	<u>8.7</u>	<u>16.7</u>	<u>9.9</u>	<u>10.7</u>	<u>5.7</u>	10.7	8.0
Chlorite	<u>2.9</u>	<u>5.3</u>	<u>2.9</u>	<u>5.0</u>	<u>2.0</u>	<u>5.2</u>	<u>2.0</u>	<u>4.2</u>
Quartz	6.6	6.6	<u>6.6</u>	<u>8.2</u>	<u>27.8</u>	<u>18.1</u>	<u>27.8</u>	<u>20.5</u>
Plagioclase	8.7	9.7	<u>8.7</u>	<u>4.9</u>	<u>34.5</u>	<u>21.3</u>	<u>34.5</u>	<u>15.8</u>

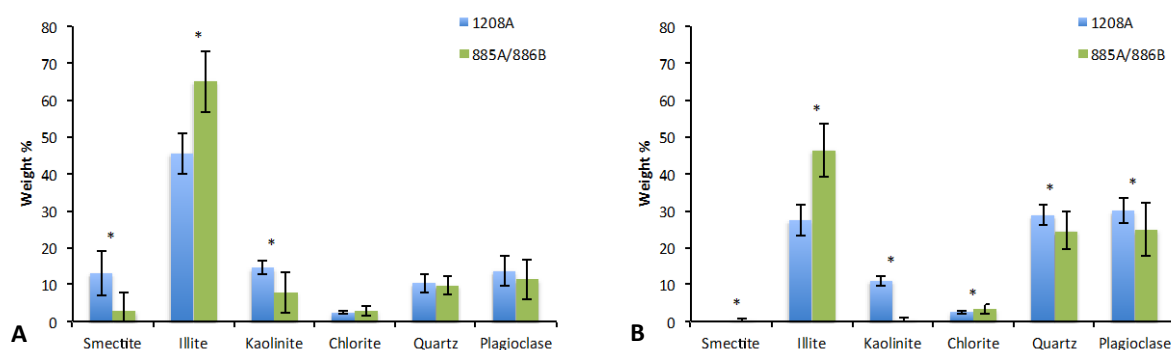


Figure 23. Average mineralogical composition of the (A) <2µm and (B) 2-20µm fraction of 885A/886B (n = 34) and 1208A sediments (n = 43). * indicates significant differences at $\alpha = 0.05$, bars = standard deviation

Table 10. Average weight % of the main mineral components of the <2µm and 2-20µm fraction in sediments from Sites 1208A and 885A/886B. Bold underlined data indicate significant differences between 1208A and 885A/886B at $\alpha = 0.05$. ND = not determined.

Mineral	Average weight %			
	<2µm		2-20µm	
	1208A (n = 43)	885A/886B (n = 34)	1208A (n = 43)	885A/886B (n = 34)
Smectite	<u>13.2</u>	<u>2.8</u>	ND	<u>0.4</u>
Illite	<u>45.5</u>	<u>65.1</u>	<u>27.5</u>	<u>46.5</u>
Kaolinite	<u>14.6</u>	<u>7.9</u>	<u>11.0</u>	<u>0.2</u>
Chlorite	2.5	2.8	<u>2.6</u>	<u>3.3</u>
Quartz	10.4	9.8	<u>28.9</u>	<u>24.6</u>
Plagioclase	13.7	11.5	<u>30.0</u>	<u>25.0</u>

5.5.1 Transportation time and distance

The differences in transportation time and distance from the Asian source regions, and subsequent varying fractionation degrees, can be reflected by several features of the results.

The transportation distance from the Asian deserts is shorter to Lingtai than to 1208A, which is consistent with Lingtai containing more quartz in all units and less kaolinite within the paleosol unit (Fig. 20, Table 7). Transportation related processes could however not explain the higher illite concentration within the paleosols at Lingtai than at 1208A. Illite might instead have an additional pedogenic origin which is supported by the conclusions of Ding *et al.*, 1999 and Gylesjö and Arnold, 2006 that states that pedogenic processes favoured by enhanced summer monsoon influence seem to have contributed to the illite concentration at the CLP. On the other hand, illite tends to get more crystalline with increased burial depth within marine sediments.

The transportation distance from Asia is longer to the ADIOS sampling station and MW sampling locations than to 1208A. This can be reflected by the higher illite and chlorite concentrations in both size fractions, and lower quartz and plagioclase concentrations in

the 2-20 μ m fraction in both dust assemblages than in the surficial 1208A sediments (Fig. 21 and 22, Table 8).

The transportation distance from Asia is also longer to 885A/886B than to 1208A. This is coherent with more chlorite, less quartz and plagioclase in the 2-20 μ m fraction, and more illite in both size fractions at 885A/886B than at 1208A (Fig. 23, Table 9).

5.5.2 Volcanic contribution

The differences in smectite and plagioclase concentrations are likely results of varying amounts of volcanic contribution, which can be suggested by the closer location of 1208A to the ash source and the presence of ash layers exclusively at 1208A.

This is consistent with the higher quartz but not plagioclase concentration within all units at Lingtai compared to 1208A. Quartz and plagioclase are similarly affected by fractionation during transportation due to their similar size and density. The higher concentration of quartz but not plagioclase at Lingtai compared to 1208A is therefore likely a result of lower ash input due to the prevailing westerlies transporting the ash over the Pacific, combined with the higher resistance of quartz than plagioclase to chemical weathering. The higher smectite concentration at 1208A than at Lingtai could be due to volcanic glass alteration in combination with relative enrichment of smectite by longer transportation (Fig. 20, Table 7).

More smectite in the <2 μ m fraction in the surficial 1208A sediments than in the MW and ADIOS dust is also probably a result of diagenetic alteration of volcanic glass, but may furthermore be contributed to under-sampling by the meshes (Blank *et al.*, 1985) and the fact that the dust compositions are each represented by a single spring dust event.

Higher smectite concentrations in the <2 μ m fraction is also observed at 1208A compared to 885A/886B (Fig. 23, Table 9), and could similarly be due to volcanic ash alteration. This is consistent with fact that none of the abundant Pleiocene-Pleistocene ash layers found at 1208A and at the other North Pacific Sites drilled during the ODP Leg 145 expedition were present at 885A or 886B (Rea *et al.*, 1998).

5.5.3 Mixing of dust from different source areas

Particular aspects of the comparative data could suggest that mixing of dust from different source areas have resulted in mineralogical differences. Transportation related fractionation cannot serve as explanation for the lack of significant differences in the primary mineral concentrations in the <2 μ m fraction between the MW dust and surficial 1208A sediments (Fig. 21A, Table 8). Arnold *et al.*, 1998 concluded that the mineralogical composition of the MW dust shifted from being mainly influenced by Asian dust, which is relatively enriched in illite, to Alaskan/Aleutian dust, which is relatively enriched in plagioclase. The Alaskan/Aleutian source areas are dominated by volcanogenic bedrock that has been altered by physical weathering processes, which makes dust from these sources relatively enriched in not just plagioclase but also quartz (Arnold *et al.*, 1998). Consequently, since the MW dust incorporated additional dust with higher primary mineral proportions of Alaskan/Aleutian origin, it may have reduced the effect of primary mineral depletion caused by the longer transportation distance from Asia.

The lower kaolinite concentration in both size fractions at 885A/886B than at 1208A might be a result of the more northern location of these sites enabling the possibility of additional contribution from a more northern source area with less favorable climatic conditions for chemical weathering processes.

6. Conclusions

The purpose of this study was to use mineralogy, obtained through XRD analyses, as a common comparative proxy to evaluate whether a similar source of the eolian sediments from Site 1208A on the central Shatsky Rise, NW Pacific Ocean, and Lingtai, central CLP could be inferred. This would allow the yet relatively poorly dated loess-paleosoil sequence to be directly linked with well-dated marine sediments, which would facilitate further dating refinements of these valuable terrestrial climatic archives without the complications of linking different proxy records. Other objectives were to investigate whether a mineralogical change could be indicated at 1208A at ~2.6 Ma, similar to what has been observed at Lingtai, and compare the mineralogical composition of the 1208A sediments with that of North Pacific mineral dust from the ADIOS and Moana Wave cruises and North Pacific sediments from Sites 885A/886B. A methodological objective was to determine if using adjustable or fixed XRD divergence slit width settings would alter the mineralogical interpretations.

Limited samples and significant volcanic contribution and alteration are likely reasons for why this study did not determine any prominent mineralogical or grain size changes in neither the <2 μ m nor 2-20 μ m fraction between the upper and lower 1208A section, or at ~2.6 Ma. More ash layers in the lower section could explain the larger grain size, lower clay and higher sand concentrations, and higher skewness values of both the <2 μ m and 2-20 μ m fraction. The more pronounced second coarse mode of the <2 μ m grain size distributions in the lower than upper section, and the changes between slightly fine and coarse skewed grain size distributions of the 2-20 μ m fraction in the lower section could likewise be due to more ash in the lower than upper section. However, this assumes that the ash particles are coarser than the mineral dust particles, which Hovan *et al.*, 1991 concluded from smear slide analyses of core V21-146, likewise retrieved from the Shatsky Rise. Disseminated ash may also have obscured the purely terrigenous signal as inferred by the lack of difference in the majority of the grain size parameters and the smectite, plagioclase and unidentified material proportions between the samples located closest to the ash layers and the remaining sample suite. Significant ash influence may be further indicated by the random or weak linear relationships between the grain size and the different mineral proportions. Future studies could benefit from analyzing the eolian bulk grain size distribution and smear slides in order to further evaluate the influence of ash.

An alternative explanation for why no substantial mineralogical changes of the eolian sediments at Site 1208A have been detected at ~2.6 Ma is that although the eolian sources were developed prior to ~2.6 Ma, the meteorological conditions caused reduced dust deposition on the CLP during the late Pliocene compared to the early Pleistocene. Dust deposition over the North Pacific Ocean would not have been precluded by these conditions. Any pronounced mineralogical responses to Asian aridification at 1208A could therefore have occurred earlier than the time period investigated in this study, as has been observed at the North Pacific Sites 885A/886B at 3.8 Ma. Prolonging the 1208A mineralogical record is therefore recommend for future studies.

Many different factors influence the mineralogy of eolian sediments, such as geology and climate of the source areas, transportation pathways and distances, and post-depositional alteration processes. For comparative studies, several factors may also affect the mineralogical similarity between sites such as different age models, resolutions, analytical and laboratory techniques. Adjustable and fixed XRD divergence slit settings have resulted in similar interpretations of average quartz and talc peak

areas for monomineralic samples in this study. The slight intensity variation of the quartz peak obtained from the five measurements reflects the instrumental variability at each slit setting, since the same quartz plate was re-measured. The intensity variations of the talc peaks are due to the filter-mounting procedure causing small differences in sample displacement.

Using mineralogy as common proxy has enabled the majority of the mineralogical differences between the compared records to be explained by different transportation distances from the Asian source areas, causing varying degrees of size and compositional fractionation of the dust assemblages, and unequal volcanic input. Contribution of Alaskan/Aleutian dust during the later part of the Moana Wave cruise, and possibly additional dust input to Sites 885A/886B from more northern sources could also be indicated by the mineralogical comparisons. This study may infer similar origin of the eolian sediments from 1208A and Lingtai since the closer location of Lingtai to the Asian sources could explain the higher quartz concentration, and substantial ash contribution to 1208A could have caused the higher smectite concentration and reduced the differences in plagioclase concentration caused by fractionation during transportation. This study indicates that XRD-obtained mineralogy can serve as a useful proxy for directly linking the terrestrial and marine realms in future studies. This would facilitate further dating refinements of the CLP that enable high-resolution paleoclimatic studies of the East Asian monsoon system.

7. Acknowledgments

First and foremost I would like to express my sincere appreciation for my main supervisor Eve Arnold for all her valued academic guidance and personal support. I am very grateful for all the laboratory help provided by my co-supervisor Carina Johansson, and the scientific writing education by Hildred Crill. I would also like to send many thanks to my friends Sandra Gdaniec and Rebecka Åberg for their genuine interest and feedback, and to Daniel Hååg for computer support. Last but not least I would like to thank Kristoffer Hååg and my family for their never-ending encouragements.

8. References

Amo, M., and Minagawa, M., 2003. Sedimentary record of marine and terrigenous organic matter delivery to the Shatsky Rise, western North Pacific over the last 130 kyr. *Organic Geochemistry*, 34: 1299-1312.

Arnold, E., Leinen, M., and King, J., 1995. Paleoenvironmental variations based on the mineralogy and rock-magnetic properties of sediment from Sites 885 and 886. In Rea, D.K., Basov, L.A., Scholl, D.W., and Allan, J.F., (Eds.), *Proceedings of the Ocean Drilling program, Scientific Results*, 145: 231-245.

Arnold, E., Merrill, J., Leinen, M. and King, J., 1998. The effect of source area and atmospheric transport on mineral aerosol collected over the North Pacific Ocean, *Global and Planetary Change*, 18: 137-159.

Biscaye, P.E., 1965. Mineralogy and Sedimentation of Recent Deep-sea Clay in the Atlantic Ocean and Adjacent Areas and Oceans. *Geological Society of America Bulletin*, 7: 803-832.

Blank, M., Leinen, M. and Prospero, J.M., 1985. Major Asian aeolian inputs indicated by the mineralogy of aerosols and sediments in the western North Pacific. *Nature*, 314: 84-86.

Blauuw, M., 2012. Out of tune: the danger of aligning proxy archives. *Quaternary Science Reviews*, 36: 38-49.

Bown, P.R., 2005. Cenozoic calcareous nannofossil biostratigraphy, ODP Leg 198 Site 1208 (Shatsky Rise, northwest Pacific Ocean). In Bralower T.J., Premoli Silva L., Malone M.J., et al., *Proceedings of the Ocean Drilling Program, Scientific Results*, 198: 1-44.

Breitenbach, S.F.M, Rehfeld, K., Goswami, B., Baldin, J.U.L., Ridley, H.E., Kennett, D.J., Pruber, K.M., Aquino, V.V., Asmerom, Y., Polyak, V.J., Cheng, H., Kurths, J., and Marwan, N., 2012. CONstructing Proxy Records from Age models (COPRA). *Climate of the Past*, 8: 1765-1779.

Chamley, H., 1989. *Clay Sedimentology*, 1st edition, Springer-Verlag, Berlin. 623 pp.

Chipera, S.J and Bish D.L., 2013. Fitting Full X-Ray Diffraction Patterns for Quantitative Analysis: A Method for Readily Quantifying Crystalline and Disordered Phases. *Advances in Materials Physics and Chemistry*, 3: 47-53.

Das, S.S, Rai, A.K., Akaram, V., Verma, D., Pandey, A.C., Dutta, K., and Prasad, G.V.R., 2013. Paleoenvironmental significance of clay mineral assemblages in the southeastern Arabian Sea during last 30 kyr. *Journal of Earth System Science*, 122: 173-185.

Dickens, G.R., Snoeckx, H., Arnold, E., Morley, J.J., Owen, R.M., Rea, D.K., and Ingram, L., 1995. Composite depth scale and stratigraphy for sites 885/886. In Rea, D.K., Basov, I.A.,

Scholl, D.W., and Allen, J.F., *Proceedings of the Ocean Drilling Program, Scientific Results*, 145: 205-217.

Ding, Z.L., Rutter, N., Han, J.T., and Liu, T.S., 1992. A coupled environmental system formed about 2.5 Ma over eastern Asia. *Palaeogeography, Palaeoclimatology, Palaeoecology*, 94: 223-242.

Ding, Z.L., Yu, Z.W., Rutter, N.W., Liu, T.S., 1994. Towards an orbital time scale for Chinese loess deposits. *Quaternary Science Reviews*, 13: 39-70.

Ding, Z.L., Derbyshire, I.E., Yang, S.L., Yu, I.Z.W., Xiong, S.F., and Liu, T.S., 2002. Stacked 2.6-Ma grain size record from the Chinese loess based on five sections and correlation with the deep-sea $\delta^{18}\text{O}$ record. *Paleoceanography*, 17: 5-1—5-21.

Ding, Z.L., and Yang, S.L., 2000. C_3/C_4 vegetation evolution over the last 7.0 Myr in the Chinese Loess Plateau: evidence from pedogenic carbonate $\delta^{13}\text{C}$. *Palaeogeography, Palaeoclimatology, Palaeoecology*, 160: 291-299.

Ding, Z.L., Xiong, S.F., Sun, J.M., Yang, S.L., Gu, Z.Y., and Liu, T.S., 1999. Pedostratigraphy and paleomagnetism of a ~ 7.0 Ma eolian loess-red clay sequence at Lingtai, Loess Plateau, north-central China and the implications for paleomonsoon evolution. *Palaeogeography, Palaeoclimatology, Palaeoecology*, 152: 49-66.

Elzea, J.M., Udom, I.E., and Miles, W.J., 1994. Distinguishing well ordered opal-CT and opal-C from high temperature cristobalite by x-ray diffraction. *Analytica Chimica Acta*, 286: 107-116.

Evans, H.F., Channell, J.E.T. and Sager, W.W., 2005. Late Miocene-Holocene magnetic polarity stratigraphy and astrochronology, ODP Leg 198, Shatsky Rise. In Bralower, T.J., Premoli Silva, L. and Malone, M.J. (Eds.), *Proceedings of the Ocean Drilling Program. Scientific Results*, 198: 1-39.

Ferguson, W.S., Griffin, J.J. and Goldberg, E.D., 1970. Atmospheric Dusts from the North Pacific – A Short Note on a Long-Range Eolian Transport. *Journal of Geophysical Research*, 75: 1137-1139.

Gadley, K.L. and Marsaglia, K.M., 2005. Petrography and correlation of Cenozoic ash layers recovered on Shatsky Rise, ODP Leg 198. In Bralower, T.J., Premoli Silva, L. and Malone, M.J. (Eds.), *Proceedings of the Ocean Drilling Program. Scientific Results*, 198: 1-26.

Granberg, T., 2012. Grain size analysis – a comparison between laser and Sedigraph analytical techniques. Bachelor thesis, University of Stockholm.

Gylesjö, S., 2005. Data report: Late Pleistocene terrigenous input to Shatsky Rise, Site 1208. In Bralower T.J., Premoli Silva L. and Malone M.J. (Eds.), *Proceedings of the Ocean Drilling Program, Scientific Results*, 198: 1-7.

Gylesjö, S. and Arnold, E., 2006. Clay mineralogy of a red clay-loess sequence from

- Lingtai, the Chinese Loess Plateau. *Global and Planetary Change*, 51: 181-194.
- Heath, G.R. and Pisias, N.G., 1979. A method for the quantitative estimation of clay minerals in North Pacific deep-sea sediments. *Clays and Clay Minerals*, 27: 175-184.
- Hovan, S.A., Rea, D.K., Pisias, N.G., 1991. Late Pleistocene continental climate and oceanic variability recorded in northwest Pacific sediments. *Paleoceanography*, 6: 349-370.
- Hovan, S.A., Rea, D.K., Pisias, N.G. and Shackleton, N.J., 1989. A direct link between the China loess and marine $\delta^{18}\text{O}$ records: aeolian flux to the north Pacific. *Nature*, 340: 296-298.
- Huang, T.C., 1980. A volcanic sedimentation model: implications of processes and responses of deep-sea ashes. *Marine Geology*, 38: 103-122.
- Hull, A.W., 1919. X-ray chemical analysis, Notes from the research laboratory, General Electric Company. *Journal of Industrial & Engineering Chemistry*, 11: 1099.
- Jaccard, S.L., Haug, G.H., Sigman, D.M., Pedersen, T.F., Thierstein, H.R., and Röhl, U., 2005. Glacial/Interglacial Changes in Subarctic North Pacific Stratification. *Science*, 308: 1003-1006.
- Jones, J.B., and Segnit, E.R., 1971, The nature of opal 1. nomenclature and constituent phases, *Journal of the Geological Society of Australia: An International Geoscience Journal of the Geological Society of Australia*, 18(1): 57-68.
- Kasanin-Grubin, M., 2013. Clay mineralogy as a crucial factor in badland hillslope processes. *Catena*, 106: 54-67.
- Krylov, A.A., Andreeva, I.A., Vogt, C., Backman, J., Krupskaya, V.V., Grikurov, G.E., Moran, K., and Shoji, H., 2008. A shift in heavy and clay mineral provenance indicates a middle Miocene onset of a perennial sea ice cover in the Arctic Ocean. *Paleoceanography*, 23.
- Krüger, H., and Fischer, R.S., 2004. Divergence-slit intensity corrections for Bragg-Brentano diffractometers with circular sample surfaces and known beam intensity distribution. *Journal of Applied Crystallography*, 37: 472-476.
- Leinen, M., Prospero, J.M., Arnold, E. and Blank, M., 1994. Mineralogy of aeolian dust reaching the North Pacific Ocean 1. Sampling and analysis. *Journal of Geophysical Research*, 99(10): 21017-21023.
- Lisiecki, L.E., and Raymo, M.E., 2005. A Pliocene-Pleistocene stack of 57 globally distributed benthic $\delta^{18}\text{O}$ records. *Paleoceanography*, 20.
- Liu, T., and Ding, Z., 1993. Stepwise coupling of monsoon circulations to global ice volume variations during the late Cenozoic. *Global and Planetary Change*, 7: 119-130.
- Liu, T., and Ding, Z., 1998. Chinese Loess and the Paleomonsoon. *Annual Reviews of Earth and Planetary Sciences*, 26: 111-145.

Lu, H., Liu, X., Zhang, F., An, Z., Dodson, J., 1999. Astronomical calibration of loess-palesol deposits at Luochuan, central Chinese Loess Plateau. *Palaeogeography, Palaeoclimatology, Palaeoecology*, 154: 237-246.

McMillan, D.G., and Constable, C.G., 2006. Limitations in correlation of regional relative geomagnetic paleointensity. *Geochemistry, Geophysics, Geosystems*, 7: 1-12.

Merrill, J., Arnold, E., Leinen, M. and Weaver, C., 1994. Mineralogy of aeolian dust reaching the North Pacific Ocean 2. Relationship of mineral assemblages to atmospheric transport patterns. *Journal of Geophysical Research*, 99: 21025-21032.

Meysman, F.J.R., Middelburg, J.J., and Heip, C.H.R., 2006. Bioturbation: a fresh look at Darwin's last idea. *Trends in Ecology and Evolution*, 21: 688-695.

Moore, D.D. and Reynolds, R.C., 1997. *X-ray diffraction and the identification and analysis of clay minerals*. 2nd edition, Oxford University Press, New York. 332 pp.

Morley, J.J., Tiase, J.V.L., Ashby, M.M., Kashgarian, M., 1995. A high-resolution stratigraphy for Pleistocene sediments from the North Pacific Sites 881, 883, and 887 based on abundance variations of the radiolarian *Cycladophora davisiana*. In Rea, D.K., Basov, L.A., Scholl, D.W., and Allen, J.F. (Eds.), *Proceedings of the Ocean Drilling program, Scientific Results*, 145: 133-140.

Muhs, D.R., 2013. The geologic records of dust in the Quaternary. *Aeolian Research*, 9: 3-48.

Panda, A.K., Mishra, B.G., Mishra, D.K., and Singh, R.K., 2010. Effect of sulphuric acid treatment on the physico-chemical characteristics of kaolin clay. *Colloids and Surfaces A: Physicochemical and Engineering Aspects*, 363: 98-104.

Patterson, D.B., Farley, K.A., and Norman, M.D., 1999. ⁴He as a tracer of continental dust: A 1.9 million year record of aeolian flux to the west equatorial Pacific Ocean. *Geochimica et Cosmochimica Acta*, 63: 615-625.

Petschick, R., 2010. MacDiff 4.2.6 software, accessed through <http://www.geol-pal.uni-frankfurt.de/Staff/Homepages/Petschick/Classicsoftware.html>.

Poppe, L.J., Commeau, J.A. and Pense, G.M., 1989. Effect of chlorine in clay-mineral specimens prepared on silver metal-membrane mounts for X-ray powder diffraction analysis. *Clays and Clay Minerals*, 37: 381-384.

Prospero, J.M., 1981. Eolian transport to the World Ocean. *The Oceanic Lithosphere, The Sea*, 7: 801-874.

Rack, F.R., Janecek, T.R., Erba, E., Fenner, J., and Gee, J.S., 1995. Synthesis of Terrigenous accumulation rates and biostratigraphic studies at sites in the Northwestern Pacific Ocean, with comparisons to adjacent regions of the Pacific Gyre. In Haggerty, J.A., Premoli, S.I., Rack, F., and McNutt, M.K. (Eds.), *Proceedings of the Ocean Drilling Program, Scientific Results*, 144: 691-736.

Rea, D.K., 1994. The paleoclimatic record provided by eolian deposition in the deep sea: the geologic history of wind. *Reviews of Geophysics*, 32: 159-195.

Rea, D.K., Snoeckx, H., and Joseph, L.H., 1998. Late Cenozoic eolian deposition in the North Pacific: Asian drying, Tibetan uplift, and cooling of the northern hemisphere. *Paleoceanography*, 13: 215-224.

Robinson, S.A., and Jenkyns, H.C., 2005. Data report: Opal and carbonate data from the Miocene to Lower Pliocene, Site 1208 (Central High, Shatsky Rise). In Bralower, T.J., Premoli Silva, L., and Malone M.J. (Eds.), *Proceedings of the Ocean Drilling Program, Scientific Results*, 198: 1-7.

Sager, W.W., Zhang, J., Korenaga, J., Sano, T., Koppers, A.A.P., Widdowson M., Mahoney J.J., 2013. An immense shield volcano within the Shatsky Rise oceanic plateau, northwest Pacific Ocean. *Nature Geoscience*, 6: 976-981.

Scudder, R.P., Murray, R.W., and Plank, T., 2009. Dispersed ash in deeply buried sediment from the northwest Pacific Ocean: An example from the Izu-Bonin arc (ODP Site 1149), *Earth and Planetary Science Letters*, 284: 639-648.

Shipboard Scientific Party, 2002. Explanatory Notes. In Bralower, T.J., Premoli Silva, L., Malone, M.J., et al., *Proceedings of the Ocean Drilling Program, Initial Reports*, 198: 1-63.

Shipboard Scientific Party, 2002. Site 1208A. In Bralower, T.J., Premoli Silva, L., Malone, M.J., et al., *Proceedings of the Ocean Drilling Program, Initial Reports*, 198: 1-93.

Shipboard Scientific Party, 1993, Sites 885/886, In Rea, D.K., Basov, I.A., Janecek, T.R., Palmer-Julson, A., et al., *Proceedings of the Ocean Drilling Program, Initial Reports*, 145: 303-334.

Singh, V., and Agrawal, H.M., 2012. Qualitative soil mineral analysis by EDXRF, XRD and AAS probes. *Radiation Physics and Chemistry*, 81: 1796-1803.

Smith, C.R., and Rabouille, C., 2002. What controls the mixed-layer depth in deep-sea sediments? The importance of POC flux. *Limnology and Oceanography*, 47(2): 418-426.

Sterlitech Corporation 2013, Frequently Asked Questions, Silver Membranes, <http://www.sterlitech.com/faqs/silver-membranes>. Accessed 16 October 2013.

Sun, D., Su, X., Bloemendal, J., and Lu, H., 2008, Grain-size and accumulation rate records from Late Cenozoic aeolian sequences in northern China: Implications for variations in the East Asian winter monsoon and westerly atmospheric circulation. *Palaeogeography, Palaeoclimatology, Palaeoecology*, 264: 39-53.

Teal, L.R., Bulling, M.T., Parker, E.R., and Solan, M., 2008. Global patterns of bioturbation intensity and mixed depth of marine soft sediments. *Aquatic Biology*, 2: 207-218.

Uematsu, M., Duce, R.A., Prospero, J.M., Chen, L., Merrill, J.T. and McDonald, R.L., 1983. Transport of Mineral Aerosols From Asia Over the North Pacific Ocean. *Journal of*

Geophysical Research, 88: 5343-5352.

Van der Gaast, S., 1991. Mineralogical analysis of marine particles by X-ray powder diffraction. In *Marine Particles: Analysis and Characterization*. Geophysical Monograph 63, American Geophysical Union, Washington, DC, 343-362 pp.

Varadachari, C., Goswami, G., and Ghosh, K., 2006. Dissolution of Iron Oxides. *Clay Research*, 25: 1-19.

Venti, N.L., 2011. The role of the Kuroshio Extension in the Pliocene-Pleistocene climate transition, PhD thesis, University of Delaware, USA.

Venti, N.L. and Billups, K., 2012. Stable-isotope stratigraphy of the Pliocene-Pleistocene climate transition in the northwestern subtropical Pacific. *Palaeogeography, Palaeoclimatology, Palaeoecology*, 326-328: 54-65.

Vogt, C., 2009. Data report: semiquantitative determination of detrital input to ACEX sites based on bulk sample X-ray diffraction data. In Backman, J., Moran, K., McInroy, D.B., Mayer, L.A., and the Expedition 302 Scientists, *Proceedings of the Integrated Ocean Drilling Program*, 302.

Wang, X., Sun, D.H., Wang, F., Li, B.F., Wu, S., Guo, F., Li, Z.J., Zhang, Y.B., and Chen, F.H., 2013, A high-resolution multi-proxy record of late Cenozoic environment change from central Taklimakan Desert, China. *Climate of the Past*, 9: 2731-2739.

Wang, X., Xia, D., Zhang, C., Lang, L., Hua, T., and Zhao, S., 2012. Geochemical and magnetic characteristics of fine-grained surface sediments in potential dust source areas: Implications for tracing the provenance of aeolian deposits and associated palaeoclimatic change in East Asia. *Palaeogeography, Palaeoclimatology, Palaeoecology*, 323-325: 123-132.

Webb, P.A., and Orr, C., 1997. *Analytical Methods in Fine Particle Technology*, Micromeritics Instruments Corporation, Norcross, GA USA. 325 pp.

White, R.J., Spinelli, G.A., Mozley, P.S., and Dunbar, N.W., 2011. Importance of volcanic glass alteration to sediment stabilization: offshore Japan. *Sedimentology*, 58: 1138-1154.

Xiao, G., Zong, K., Li, G., Hu, Z., Dupont-Nivet, G., Peng, S., and Zhang, K., 2012. Spatial and glacial-interglacial variations in provenance of the Chinese Loess Plateau. *Geophysical Research Letters*, 39.

Yancheva, G., Nowaczyk, N.R., Mingram, J., Dulski, P., Schettler, G., Negendank, J.F.W., Liu, J., Sigman, D.M., Peterson, L.C., and Haug, G.H., 2007. Influence of the intertropical convergence zone of the East Asian monsoon. *Nature*, 445: 74-77.